ORNL/TM-2024/3454

Liquid Piston with Spray Cooling Near-Isothermal Compressor

Joseph Rendall
Duy Thien Nguyen
Praveen Cheekatamarla
Aaron Thornton
Stephen Kowalski

August 2024

OAK RIDGE National Laboratory

ORNL IS MANAGED BY UT-BATTELLE LLC FOR THE US DEPARTMENT OF ENERGY

ORNL/TM-2024/3454

Buildings and Transportation Science Division

LIQUID PISTON WITH SPRAY COOLING NEAR-ISOTHERMAL COMPRESSOR

Joseph Rendall
Duy Thien Nguyen
Praveen Cheekatamarla
Aaron Thornton
Stephen Kowalski

August 2024

Prepared by
OAK RIDGE NATIONAL LABORATORY
Oak Ridge, TN 37831
managed by
UT-BATTELLE LLC
for the
US DEPARTMENT OF ENERGY
under contract DE-AC05-00OR22725

CONTENTS

LIST OF FIGURES

LIST OF ABBREVIATIONS

ASME	American Society of Mechanical Engineers
CFD	computational fluid dynamics
COP	coefficient of performance
CV	check valve
DAQ	data acquisition
FM	flow meter
GUI	graphical user interface
LES	large eddy simulation
LPC	liquid-piston compressor
LS	level sensor
NI	National Instruments
ORNL	Oak Ridge National Laboratory
P-h	pressure–enthalpy
P-v	pressure–specific volume
P&ID	piping and instrument diagram
PG	propylene glycol
PR	pressure regulator
PT	pressure transducer
RANS	Reynolds-averaged Navier–Stokes
SGS	subgrid scale
SIMPLE	Semi-Implicit Method for Pressure-Linked Equations
SME	subject matter expert
TAB	Taylor analogy breakup
TC	thermocouple
URANS	unsteady Reynolds-averaged Navier–Stokes
VOF	volume of fluid
WALE	wall-adapting local eddy-viscosity
WT	watt transducer

ABSTRACT

The goal of this project was to prototype and characterize the performance of a liquid-piston spray-cooled gas compressor. The working principle of the compressor enables optimized high-efficiency operation over a very wide range of operating conditions, unlike conventional compressors that are optimized for a narrow range of operating conditions. The compressor technology is suitable for many applications, such as gas pipeline transport, gas storage, and commercial and residential heat pumps. Both physical testing and computational fluid dynamics (CFD) modeling of the processes using the Oak Ridge National Laboratory high-performance computing center were completed. The experimental and CFD studies focused on a near-isothermal liquid-piston compressor (LPC) that uses propylene glycol to compress CO_2.

The first prototype demonstrated isothermal operation during several sequentially executed cycles of CO_2 compression and raised the temperature of the compressed CO_2 by only 2 K, compared with approximately 6 K when the gas was compressed non-isothermally. Isothermal operation was demonstrated at CO_2 flow rates of up to 2 L/min. The second prototype was designed with two compression chambers to allow continuous flow of high-pressure CO_2. However, the design of the valve train to direct flow between the compression chambers was not sufficient to allow demonstration of CO_2 compression.

Numerical simulations of the LPC in which the compression chamber was filled with propylene glycol injected from the bottom inlet were performed using large eddy simulation (LES) with the wall-adapting local eddy-viscosity subgrid-scale model coupled with the multiphase volume of fluid (VOF) model to simulate the transient interface between gas and liquid and to capture the heat and mass transfers within the compression chamber. In this effort, the effects of boundary conditions applied to the LES-VOF calculations (i.e., no wall, an adiabatic wall, and a wall with a heat flux subscribed) on the overall pressure and temperature of the CO_2 gas as well as the transient evolution of flow and heat transfer within the compression chamber were investigated and are discussed in this report. The LES calculation with no wall showed no dynamical flow patterns, and the volume-averaged temperature of CO_2 increased from 305 to 392.7 K, whereas LES calculations with a constant wall temperature or a wall heat flux had similar increases of CO_2 temperatures. The results of the LES simulation using a wall heat flux showed different stages in the compression process and revealed dynamical formation and interaction of CO_2 gas layers and circulation flow patterns within the chamber that contributed to the overall heat transfer between the solid wall, gas, and liquid surface in the compressor.

Though an industrial partnership for commercializing the compressor was not secured, the technology was attractive for an industrial partner to use in two research proposals in response to US Department of Energy funding opportunity announcements.

1. INTRODUCTION

Each year in the United States, residential and commercial heating and cooling use 4.4 quads of primary energy and are responsible for 148 Mt of CO_2 emissions. Extensive efforts have been made to increase the efficiency of residential and commercial air conditioners and heat pumps.

The compressor in a vapor compression cycle, which is commonly used for residential space heating and cooling, increases the pressure and the saturation temperature of the refrigerant from the evaporator level to the level required in the condenser. Compression in conventional compressors is performed at high speed with very short residence time for the gas to exchange heat with its surroundings. This results in large viscous dissipation and high discharge temperatures. In vapor compression cooling devices, the superheated refrigerant discharged from the compressor rejects its heat to the ambient in the condenser. Because of the low overall heat transfer coefficient of refrigerant-air heat exchangers, a higher approach temperature difference is required. However, increasing the approach temperature difference increases the compressor lift and lowers the efficiency of the compressor and the refrigeration cycle. Furthermore, conventional heat pump compressors cannot compress two-phase refrigerants because of damage caused by pitting due to wet vapors. This limitation lowers the thermodynamic limit of the maximum achievable coefficient of performance (COP) of a vapor compression cycle as it departs from the ideal Carnot limit, which is based on two-phase compression.

To address these challenges, the US Department of Energy's Oak Ridge National Laboratory (ORNL) developed a near-isothermal liquid-piston compressor (LPC) that uses propylene glycol (PG) to compress CO_2. In the current design, liquid PG can enter the compression chamber in one or both of two ways, either of which creates a liquid piston for compression: from the bottom inlet or from the spray nozzle at the top of the chamber.

A near-isothermal LPC works by compressing the gas inside a compression chamber using a rising liquid column. Spraying the liquid into the chamber provides a large surface area for heat exchange. Because of the large heat transfer rate between the gas being compressed and the compression liquid, the compression process occurs almost entirely at the temperature of the sprayed liquid, which remains constant and is the source of the near-isothermal condition. This approximates a mechanical piston slowly rising in a reciprocating compressor but with much lower friction losses while removing all the heat of compression. Because the moving boundaries inside the compression chamber are hydraulic boundaries, the LPC is not limited to compressing only the gaseous phase and can compress saturated vapors. The pumped liquid is then cooled by ambient air in a heat exchanger with a much smaller surface area than a refrigerant-air heat exchanger. The implications for vapor compression refrigerating systems are significant. The LPC can be designed so the condensation occurs inside the compression chamber without the need for the refrigerant to reject heat to ambient air in a condenser. This advantage is especially beneficial to transcritical CO_2 refrigeration systems. The CO_2 can be simultaneously compressed and cooled inside the LPC, and a gas cooler may no longer be needed. Compared with a traditional solid piston, the LPC offers major advantages: it avoids gas leakage and reduces dissipation owing to friction, yielding an overall higher efficiency (Van de Ven and Li 2009; Neu, Solliec, and Santos Piccoli 2020).

Several studies have examined the use of sprayed droplets and similar concepts for achieving isothermal compression. Gerstmann and Hill (1986) performed an analytical study of increasing the efficiency of a refrigeration process by isothermalization of compression. In that work, the refrigerant was cooled by an externally cooled aerosol. The aerosol then became the liquid piston that compressed the refrigerant. The authors noted that for the aerosol, the droplets and the surface area must be small to transfer the heat stored in the liquid to the working gas.

Van de Ven and Li (2009) created a computer model of a liquid-piston concept designed to improve the efficiency of gas compression and expansion and found that greater efficiency could be achieved by using a larger quantity of small-diameter compression cylinders, improving the heat transfer while minimizing the viscous flow forces. Although the study did not specifically involve droplet-spray heat transfer, several items were noted as necessary for successful liquid-piston compression. First, a portion of the gas will diffuse in the liquid, possibly reducing the liquid's bulk modulus. This change can be avoided by designing the chamber to minimize liquid splashing, by selecting a fluid with low gas solubility, or by using a bladder to separate the liquid and the gas physically. Furthermore, the liquid should not be allowed to leave the compression chamber during the gas exhaust stroke.

Odukomaiya et al. (2016) performed computer modeling and experiments to study spray cooling to improve the round-trip efficiency of a hydropneumatic energy storage system using an LPC and direct-contact heat exchanger for waste heat recovery. The researchers found that both spray cooling during compression and waste heat utilization during expansion improved efficiency. Indicated efficiency—defined by the researchers as the work output divided by the work input—which includes only the thermodynamic losses, increased from 0.90 to 0.96, whereas the electrical efficiency, which includes all loses, increased from 0.66 to 0.70.

In a study of the compression of air using a water piston, Patil, Acharya, and Ro (2020) used a compression ratio of approximately 2.5 at injection pressures varying from 10 to 70 psi (69 to 483 kPa) and spray angles of 60°, 90°, and 120°. They defined isothermal efficiency to express how closely the compression process follows an isothermal trajectory and attributed the wide spray angle's reduced efficiency to the droplets colliding with the walls of the chamber, which rendered them unavailable to participate in heat transfer.

The concept of compression cooling via liquid droplets has also been applied to compressed-air energy storage aiming to achieve near-isothermal operations via efficient thermal management of heat release and supply (Zhou et al. 2019; Gouda et al. 2022). Compared with traditional approaches of enhancing heat transfer during compression or expansion, such as using water jackets, droplet heat transfer can be applied inside the gas chamber and hence can be much more direct and effective. Therefore, spray cooling may be an excellent option for compressed-air energy storage because conventional near-adiabatic compression can be inefficient.

Qin and Loth (2014) and Qin et al. (2014) performed numerical simulations of an LPC using droplets and reported that the droplets' total surface area was the most important characteristic for increasing compression efficiency. These authors also found that small droplets and high mass loading—defined as the ratio of the mass of water injected into the chamber to the mass of air already in the chamber—were optimal, which agrees with the conclusions of Gerstmann and Hill (1986).

Most previous studies have been performed to investigate the evolution of global temperature and pressure within the gas volume. Only a few studies have aimed to characterize the thermal fluid phenomena that occur within the compression chamber. Most numerical studies on LPCs have been performed on a 2D domain to reduce computational costs, which are high for 3D simulations.

Zhang et al. (2012) and Zhang et al. (2013) performed 2D numerical simulations of an air compressor using water and found that lower than theoretically expected heat transfer rate and compression efficiency were caused by a high liquid injection rate and high piston velocity. A high Reynolds number at high piston speeds also contributed to the lower heat transfer rate during the compression process and thus the lower compression efficiency. Similar findings were also discussed in a 2D numerical study featuring a moving boundary of a solid piston (Schober, Deichsel, and Schlucker 2016).

Gouda et al. (2022) stated that the spatial simplifications applied in 2D simulations limit the capability to correctly capture the complex and dynamically evolving thermo-hydrodynamic behaviors of the gas flow within the compressor volume. The authors argued that the flow patterns within the chamber possess the 3D

nature of flow structures and local turbulence that cannot be simulated in 2D calculations. Furthermore, Shah and Sekulic (2003) stated that 2D simulations double the compactness ratio compared with 3D geometry and underestimate the heat exchange between the wall and fluids inside the chamber, further altering the gas flow patterns. Therefore, 3D simulations of an LPC are necessary to characterize the thermo-hydrodynamic behaviors within the compression chamber (Tuhovcak, Hejcik, and Jicha 2015; Gouda et al. 2021; Gouda et al. 2022).

In summary, some of the issues that the literature demonstrates with using droplet heat transfer and an LPC are instabilities at the interface of the liquid and gas that disturb the compressing fluid, gas diffusion in liquid reducing the effectiveness of compression, liquid entrainment in the gas exiting from the discharge port, selection of compression fluid to minimize reaction and dissolution between the gas and liquid, and changes in inlet pressure and spray angle that affect the efficiency of compression. This paper presents a preliminary experimental evaluation of a CO_2 LPC. The project used recent ORNL-developed technological innovations that facilitate advanced gas/refrigerant compression with potential applications across a wide range of energy systems and devices, including vapor compression heating and cooling, industrial compressed-air distribution, CO_2 compression and storage, hydrogen compression and storage, and more. The two core innovations leveraged in this project were liquid-piston compression and advanced heat transfer via sprayed droplets. These innovations were combined with a third: a novel variable-stroke liquid compression, which (1) resulted in near-isothermal compression, improving the compression efficiency from approximately 17% to approximately 30%; (2) enabled very efficient and simple part load operation; and (3) enabled an adjustable and on-demand compression ratio and temperature ratio to facilitate switching between sensible/latent-load vs. sensible-load-only operation.

2. EXPERIMENTAL RESULTS

The concept was proven by the research team through experiments using a prototype with a single compression chamber. Results of testing demonstrated the potential for isothermal compression of CO_2. However, the flow was not steady because the compression chamber needed to be refilled with low-pressure CO_2 after each discharge cycle. Therefore, a second prototype was designed and built with two compression chambers and an accumulator chamber. The intention was that the second prototype would be able to produce a steadier flow of high-pressure CO_2. Further improvements between the first and second prototype were as follows:

- A piston cylinder configuration was added to control flow between the two compression chambers to increase control of the system and recovery energy during decompression.
- The mass of the chamber was reduced to improve the measurement of the gas temperature during non–steady state operation.
- The multiple ports on top of the first prototype chamber were replaced with a single port with a header to accept the different flows for the second prototype chambers.

2.1 FIRST PROTOTYPE: SINGLE COMPRESSION CHAMBER

Design and fabrication of the compression chamber for the first prototype were completed using the ORNL pressure systems subject matter expert's (SME's) approved design. Design drawings of the compression chambers were developed and are shown in Figure 1 and Figure 2. Pipe connections for gas inlet and discharge, compression liquid inlet, and the spray nozzle were machined into the cover of the compression chamber as shown in Figure 3. A photo of the compression chamber alone is shown in Figure 4. A pressure test per American Society of Mechanical Engineers (ASME) Section VIII UG-99 (Mechanical Engineers 2021) was performed by the manufacturer. The piping and instrument diagram (P&ID) for the first prototype is shown in Figure 5. Additionally, several changes were made to the P&ID early to account for different testing modes. The relief valve was moved from the compression chamber to the compression-liquid line to avoid freezing the valve if activated. A compression-liquid line was added so the liquid could be admitted into the compression chamber from the bottom. This allowed testing of the compressor in isentropic mode in addition to isothermal mode (admitting liquid into the top through the spray nozzle).

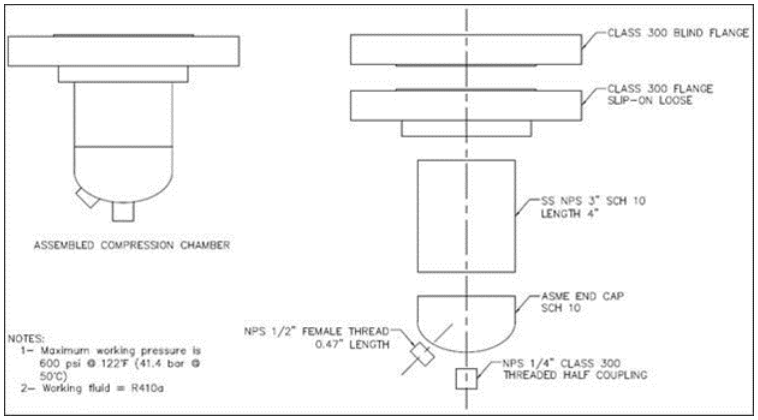

Figure 1. Makeup of the compression chamber for the first prototype.

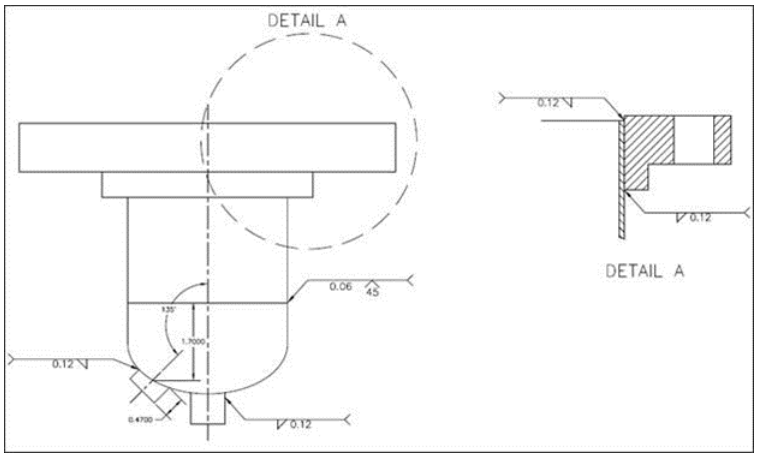

Figure 2. Weld designations to assemble the compression chamber for the first prototype.

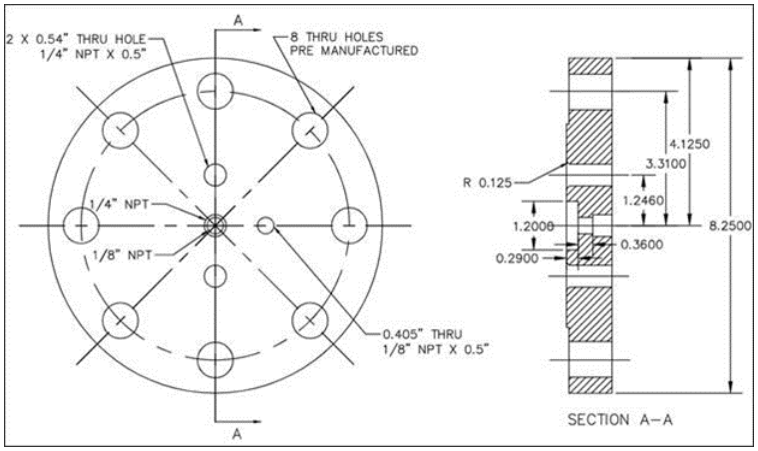

Figure 3. Hydraulic connections machined into the cover of the compression chamber for the first prototype.

Figure 4. Fabricated compression chamber for the first prototype.

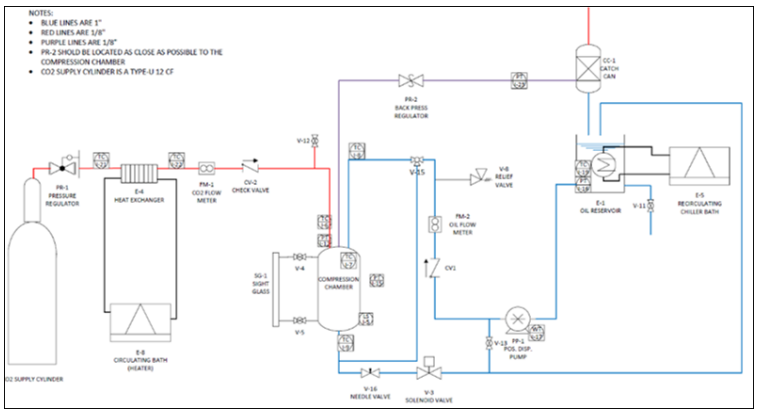

Figure 5. P&ID of the experimental facility for the first prototype.

An operational flow chart was developed based on the intended operation and control of the first prototype. This was then used to develop a data acquisition and system control scheme as follows. This scheme references the components in the P&ID by their labels. The compression process involves the steps described in Sections 2.1.1–2.1.4.

2.1.1 Intake Stroke

During the first operation, because no CO_2 or oil is in the chamber and the pressure in the chamber is below 20 bar, a pressure regulator (PR) (PR-1) opens, allowing CO_2 to flow from the CO_2 supply cylinder to the compression chamber. As CO_2 flows and expands, its temperature and pressure decrease. To prevent the temperature decrease, the E-4 heat exchanger (heater) is used to warm the flowing CO_2. Two thermocouples (TCs) (I-21 and I-22) are installed to record the CO_2 temperature before and after the heat exchanger,

respectively, so the exchanger's effect on CO_2 temperature can be determined. A flow meter (FM) (FM-1) is installed to record the CO_2 flow rate entering the compression chamber. Check valve (CV) CV-2 prevents high-pressure CO_2 or oil from flowing back toward the CO_2 supply cylinder. Valve V-12 is a venting valve installed to be used when disassembling the system. CO_2 flows until the pressure in the compression chamber reaches 20 bar. TC I-6 and pressure transducer (PT) I-12 are installed to record CO_2 temperature and pressure in the chamber. As pressure reaches 20 bar, PR-1 is closed, stopping the CO_2 flow. Solenoid valve V-3 remains closed during this step.

2.1.2 Compression Stroke

To compress with no spray cooling (isentropic compression), valve V-15 is set to open flow toward the bottom of the compression chamber. To compress with spray cooling (isothermal compression), valve V-15 is set to open flow toward the top of the compression chamber. Motor speed is set to pump PG into the compression chamber. TC I-19 and PT I-16 are installed to measure the oil temperature and level in the oil reservoir. Power input to the motor is measured by watt transducer (WT) I-17. CV-1 prevents CO_2 flow toward the pump, and FM-2 collects oil flow rate data. TC I-8 and TC I-9 are installed to collect data on the temperature of oil entering the chamber from the top and bottom of the vessel, respectively. During the compression process, while the pressure in the chamber is below 80 bar, PR-2 remains closed. Oil is continuously pumped into the chamber, compressing CO_2 as the oil level rises. Solenoid valve V-3 remains closed to prevent oil leakage from the bottom of the chamber. TC I-7 and PT I-15 are installed to monitor CO_2 temperature and pressure during the compression process.

2.1.3 Exhaust Stroke

As the CO_2 pressure in the chamber rises to pressures higher than 80 bar, the back-pressure regulator PR-2 opens, allowing high-pressure CO_2 to flow out of the chamber toward a catch can and to be discharged to the ambient. The catch can is designed to collect any oil that may have left the pressure chamber. Pumping is continued until no CO_2 is left in the compression chamber. Any oil collected in the catch can is returned to the oil reservoir.

2.1.4 Second Intake Stroke

When the compression chamber is full of oil, and as the compressed CO_2 is discharged out of the chamber to the ambient and the pressure falls below 20 bar, solenoid valve V-3 is opened, allowing oil flow from the chamber to the oil reservoir. PR-1 is also opened as the pressure falls below 20 bar, allowing low-pressure CO_2 to enter the vessel. Oil is discharged out of the chamber while the oil level is higher than the level sensor (LS) (LS I-5) positioned in the chamber. Because the oil exiting the chamber is hotter than the ambient, a second heat exchanger (chiller) E-5 is included in the system to extract the heat from the oil returning to the oil reservoir, decreasing the oil temperature. When the oil level falls below LS I-5, V-3 is closed. As explained before, PR-1 remains open while CO_2 pressure is less than 20 bar, and the compression steps are repeated. Valve V-11 is provided for draining purposes.

Based on this detailed process control scheme, the flow diagram shown in Figure 6 was generated to further develop automatic data acquisition (DAQ) and system control using National Instruments (NI) control modules involving analog and digital signal generation, acquisition, and processing via the LabVIEW operating system. Figure 7 shows the constructed system with all major components identified. The top section of the prototype comprised the high-pressure vessel along with valves and sensors, and the bottom section mainly comprised the compression fluid and the pump-motor assembly. Also shown in the figure are heat exchangers, plumbing and the fluid temperature controlling system. Additionally, NI hardware (NI cDAQ 9189 chassis) comprising 6 slots with 16 channels each was configured and integrated into the setup for controlling and data recording, as shown in Figure 8. The channel array and instruments were finalized,

and all necessary communications between the subsystems were verified. The final channel list is shown in Figure 8. A graphical user interface (GUI) as shown in Figure 9 was developed using LabVIEW to record the data, control the motor and solenoid, and monitor the ambient CO_2 and output warnings based on chamber pressure, temperature, and ambient CO_2 level. The user interface/display recorded the loop time for the output signals and data acquisition and displayed time-variant signals in different graphical formats depicting all the sensor readings, as shown in Figure 10. The experimental test bed responded well to the initial wet and dry test runs. Modifications were required only to ball valve 13, which was replaced with a needle valve for better control of the recirculation loop. Also, the sight-glass packing material did not allow proper sealing, and the sight glass was removed.

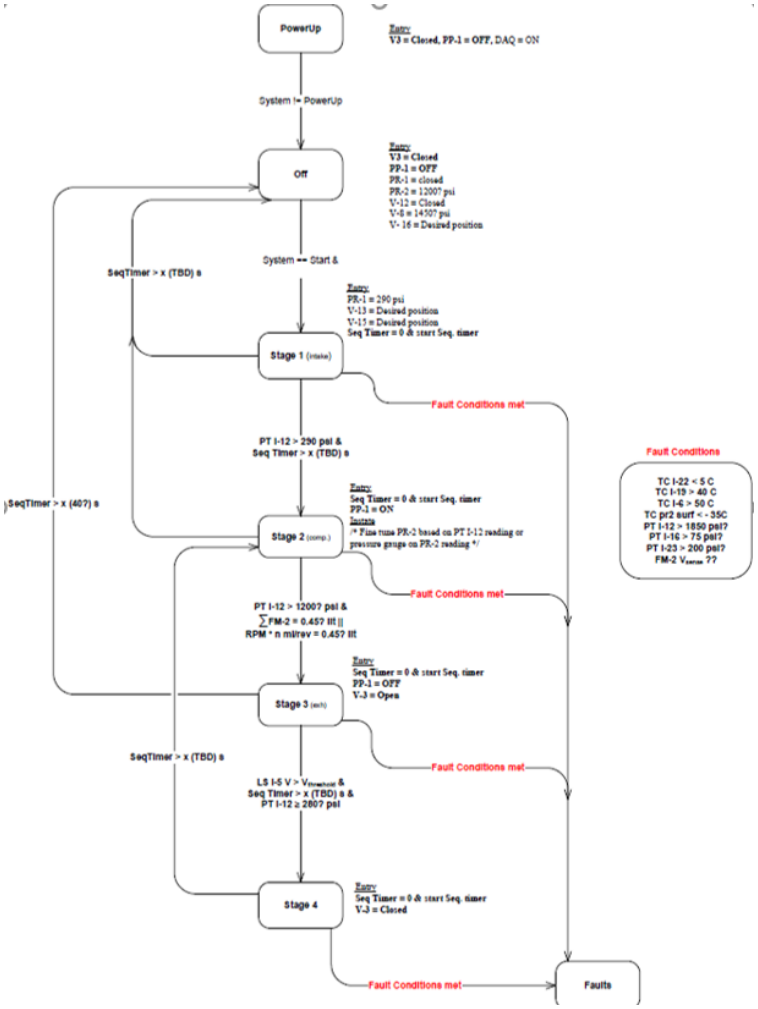

Figure 6. Flow diagram for operation of the first prototype.

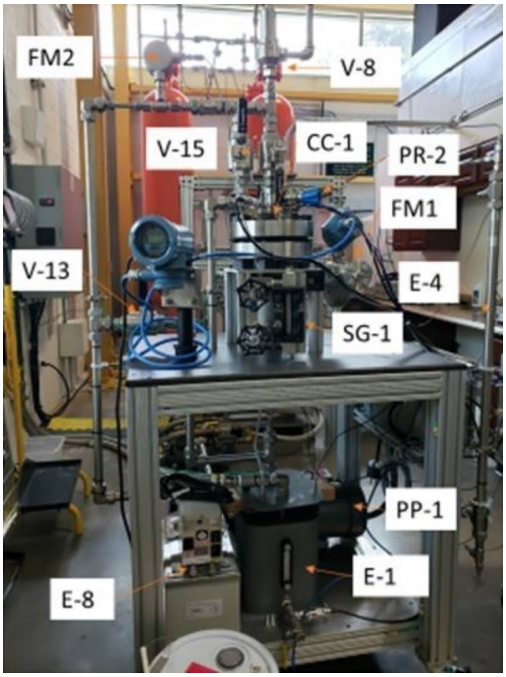

Figure 7. As-built experimental setup with selected components called out by their P&ID tags.

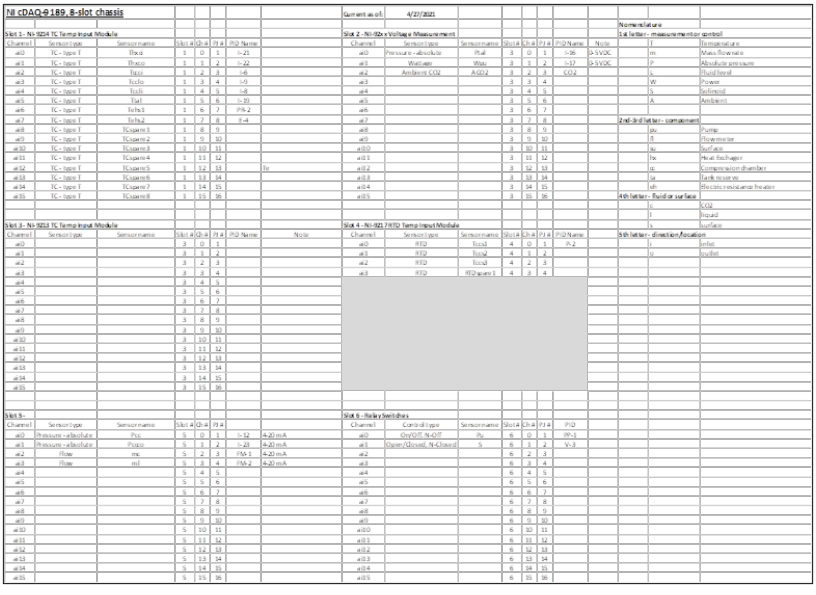

Figure 8. Screenshot of the DAQ configuration for the first prototype.

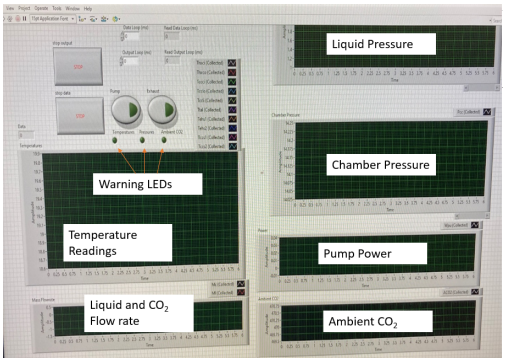

Figure 9. Graphical user interface for the first prototype.

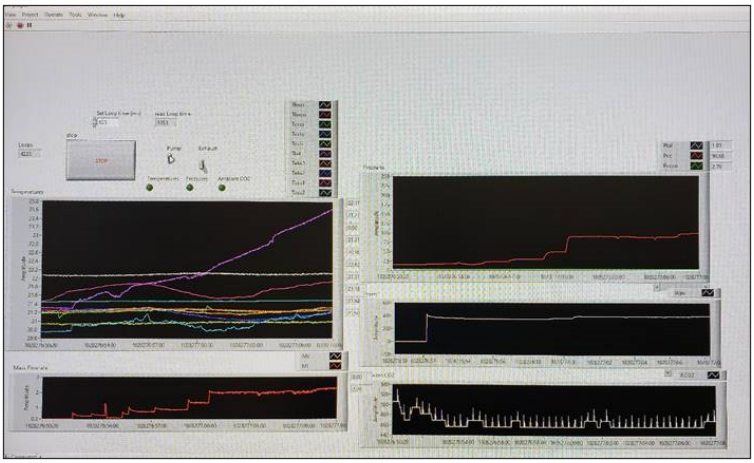

Figure 10. System communications during commissioning of the isothermal compressor system.

2.1.5 Experimental Results with the First Prototype

The initial performance evaluation of the compressor focused on its operation without the use of supplemental cooling or heating systems. In the 1 L compression vessel, the temperatures did not rise significantly during the 25 s compression cycles, suggesting the heat was removed adequately and in much larger amounts when compressed with a spray nozzle as seen in Figure 11.

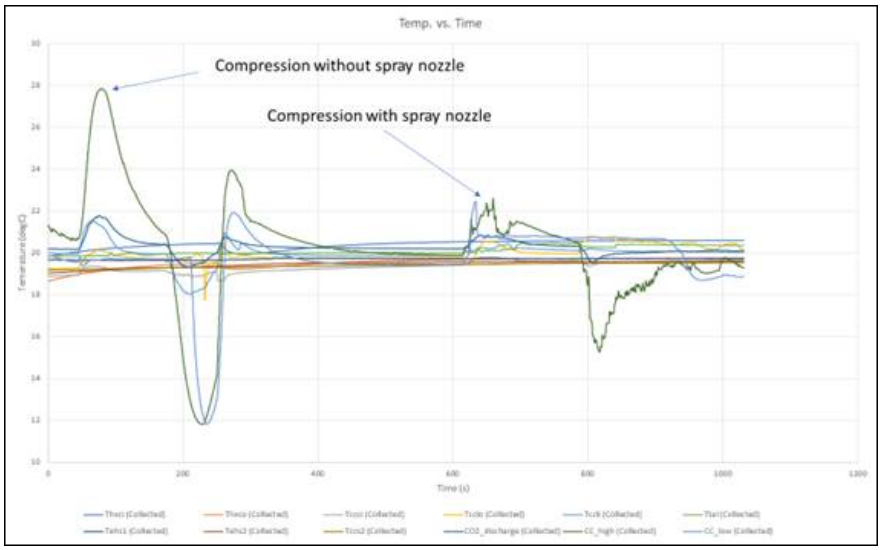

Figure 11. Initial test data from the first prototype without heating or cooling.

From the results in Figure 11, the team inferred that the CO_2 was dissolving in the PG. In the first portion of the test, during which the chamber was compressed from the bottom, the liquid outlet temperature dipped on decompression as shown by the light blue line. This may have been caused by CO_2 dissolving in the PG and leaving the chamber in solution with the PG. The relatively large decrease in temperature of the CO_2 decreased the temperature of the PG as well. Later in the same test, when the PG was sprayed from the top, resulting in a similar change in pressure during the first portion of the test, the liquid leaving the chamber continued to increase in temperature during discharge. The team theorized that the PG absorbed more heat and experienced thermal stratification in this case. Because of these perceived shortcomings of using PG for a compression fluid, the team investigated alternate compression fluids.

A promising alternative to PG is silicone oil because it is less able to dissolve CO_2. However, a safety review revealed that implementing the necessary safety controls for this fluid would necessitate extending the project timeline beyond the initial estimate. After evaluating the trade-offs, the research team determined that the observed improvement in CO_2 dissolution did not warrant the extension of the project timeline necessitated by the implementation of additional safety controls for the alternative fluid. The team continued to use PG as the compression fluid but took appropriate measures to minimize CO_2 dissolution.

The next set of tests was run with progressively higher pressures and various compression-liquid flow rates. Seven tests were conducted at different initial pressures, flow rates, and final pressures. Data are shown in Figure 12, which shows the increase in CO_2 temperature vs. pressure ratio for each test. The increase in temperature was less than 7.5 K even at pressure ratios of almost 4. For the same initial pressure, temperature, and pressure ratio, adiabatic compression would result in an approximately 70 K increase in temperature. In one test (green line in Figure 12), back pressure on the chamber was adjusted to obtain supercritical CO_2 toward the end of compression. Data for this compression are shown on a pressure–enthalpy (P-h) diagram in Figure 13, which clearly demonstrates the isothermal characteristic of this particular test. Results were recorded only for the compression of the CO_2.

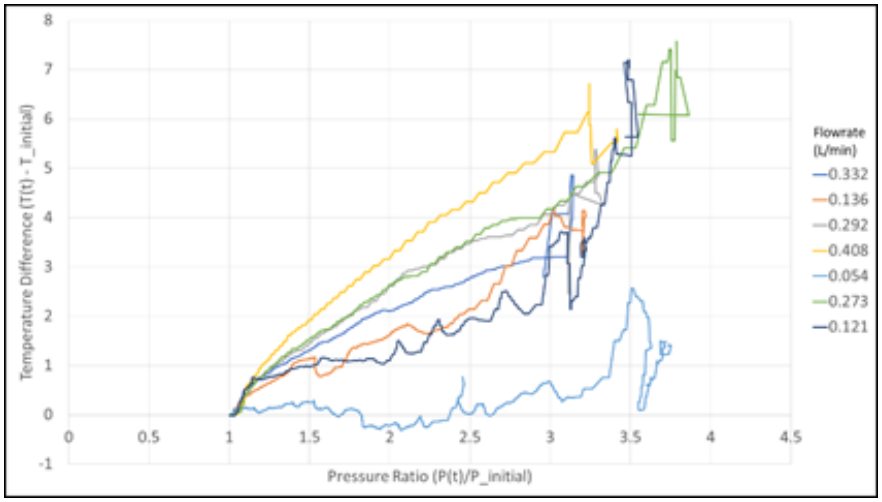

Figure 12. Increase of CO_2 temperature from its initial temperature vs. pressure ratio (measured pressure divided by initial pressure) at various flow rates.

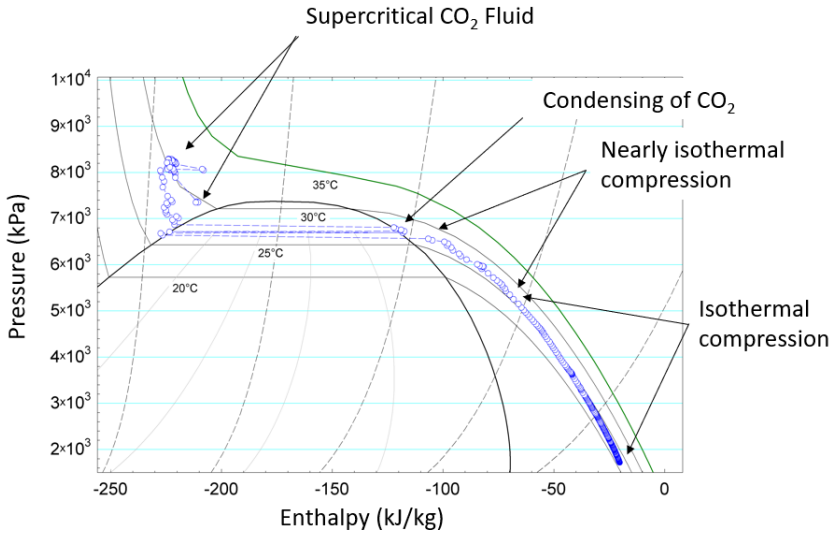

Figure 13. P-h diagram of the CO_2 in the compression chamber in test 6. Green is the target isothermal compression line. The temperature of the heat transfer fluid (HTF) was above 35°C.

The next set of experiments demonstrated compression into the supercritical regime followed by decompression back to the starting conditions. Data were again mapped to a P-h diagram as shown in Figure 14, which shows the compression (blue) and discharge (black) of the compression fluids. The compression was nearly isothermal before condensing, which is seen in the portion of the graph when the conditions of pressure and enthalpy are under the saturation curve for CO_2. The team concluded that the condensation was due to the chamber being colder than the PG (because the chamber had a relatively high thermal mass) and due to the initial temperature of the CO_2 (25°C) being too low. To alleviate these issues, the team circulated the PG through the compression chamber at 60°C before the next test to warm the chamber. Then the CO_2 gas was slowly added to the chamber through a heater to ensure no heat was lost from the chamber to condensing CO_2. This method successfully prevented condensation. The data are plotted on a pressure–specific volume (P-v) diagram in Figure 15.

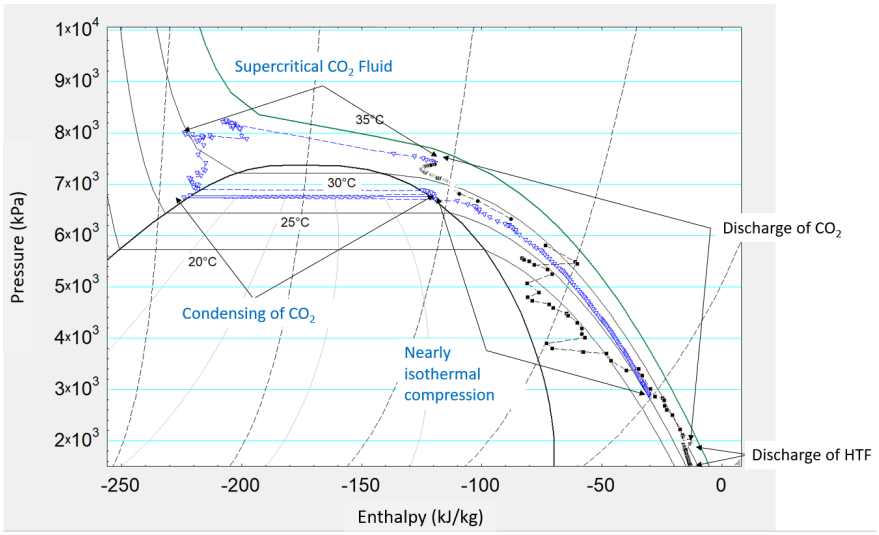

Figure 14. P-h diagram of experimental data from the first prototype operating in the supercritical region: stages of compression (purple triangles) and decompression (black squares) of experiment 7. Green is the target isothermal compression line. The temperature of the heat transfer fluid (HTF) was above 35°C.

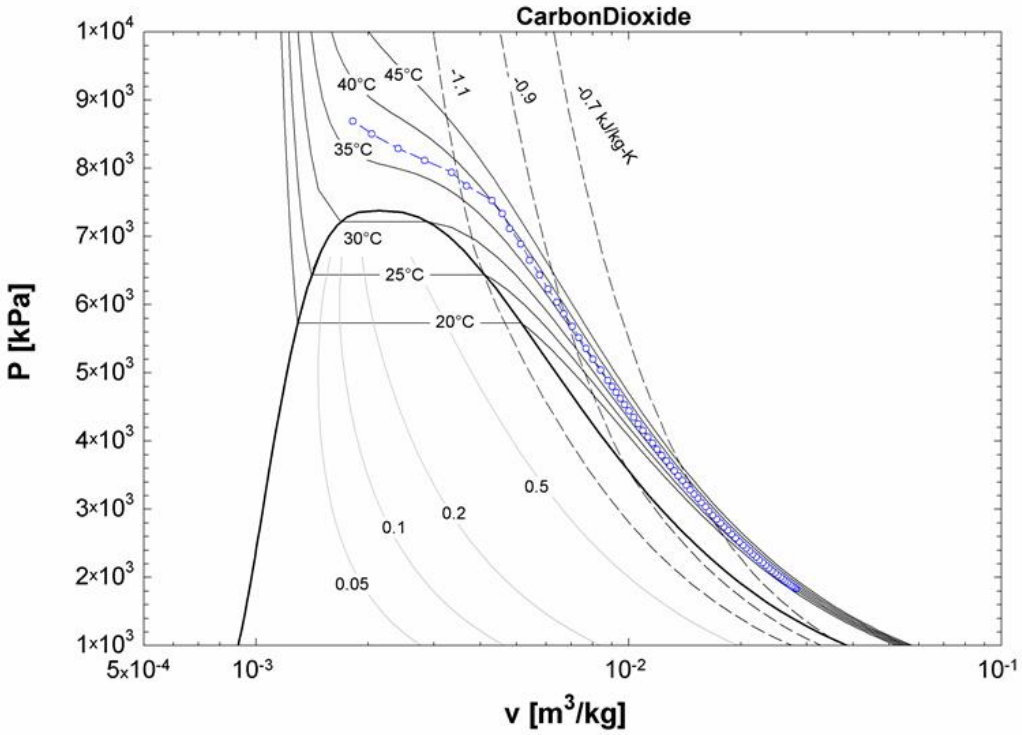

Figure 15. Pressure vs. specific volume of the compression of CO_2 showing near-isothermal compression and no condensation.

Because the previous results were single compression/decompression cycles, the team decided to complete multiple cycles in a row. Three compression cycles were run at closer-to-isothermal conditions than previous

attempts. The results are shown in Figure 16 as the three data plots (red, blue, and green) on the pressure vs. specific volume diagram. All compressions started at 250 psi (1,723 kPa). For the first compression (in blue), the target was 600 psi (4,137 kPa). The compression chamber started empty, and the rise in pressure was exponentially steady in time (i.e., the pressure rose predictably). The pressure during the second compression (in red) reached approximately 360 psi (2,500 kPa), at which point the back pressure and CO_2 were discharged to the ambient. The pressure was then reduced through the liquid discharge to 250 psi (1,723 kPa). The pressure rapidly increased during the third compression cycle (in green). This observation suggests that incomplete discharge of liquid occurred during the preceding cycle or a significant amount of CO_2 was dissolved into the liquid, which are undesirable operational conditions. A flow meter on the liquid discharge to totalize the flow discharged would be helpful in future experiments where the system is cycled by solenoid control.

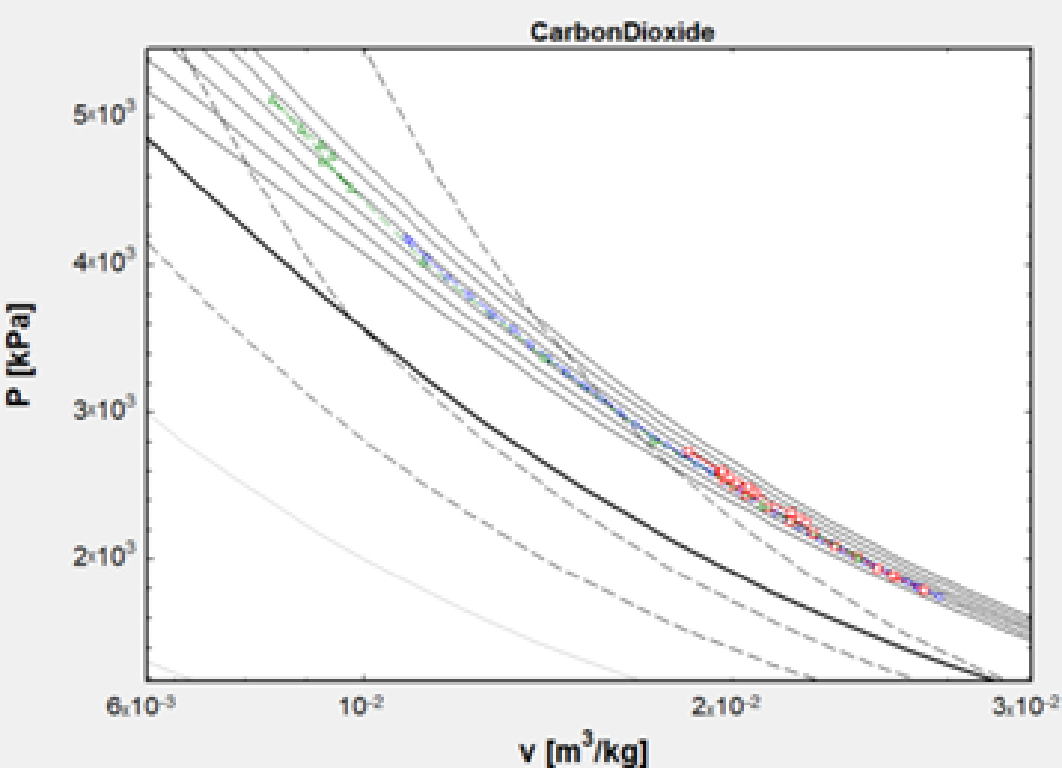

Figure 16. Pressure vs. specific volume for three compression cycles near isothermal compression: first compression (blue), second compression (red), and third compression (green).

In the next set of tests, the pressure was cycled 17 times at an average flow rate near 2 L/min. The compression stroke temperature difference vs. pressure ratio is shown in Figure 17. Generally, the chamber was warming up with the inlet temperature of the PG during the 17 successful cycles. On average, in each cycle, 0.914 L of liquid was pumped into the chamber to compress the CO_2 that was refilled from the CO_2 cylinder.

To continue observation of cycling, the compressor was then cycled at 2 L/min and 3 L/min flow rates after the chamber was prewarmed to a similar temperature as the PG. Two goals were to determine how fast the chamber could be cycled and whether the system warmed or cooled over time. The maximum speed is an indication of the limit of steady-state operation, which is an indication of the theoretical refrigerating capacity of the compressor. The temperature change over time is an indication that CO_2 may be dissolving in large amounts during compression or the mass of the chamber is absorbing the heat from the limited cycling. The change in temperature of the compressor over time is important to ensure that isothermal compression can

be reliably attained and to quantify the amount of cooling that needs to be rejected somewhere else in a system at some penalty to system performance. Figure 18, where the temperature difference of the chamber compared with the initial state vs. the pressure ratio is plotted, shows the results of six tests at a flow rate of about 2 L/min followed by three tests at 3 L/min. During the second 3 L/min compression (cycle 7), the pressure went higher than in previous cycles. The chamber cooled slightly when cycled because of the gas discharge of the CO_2 and off-gassing of CO_2 from the PG during liquid discharge to ambient pressure. The inlet temperature of the CO_2 dropped to about 21°C during liquid discharge.

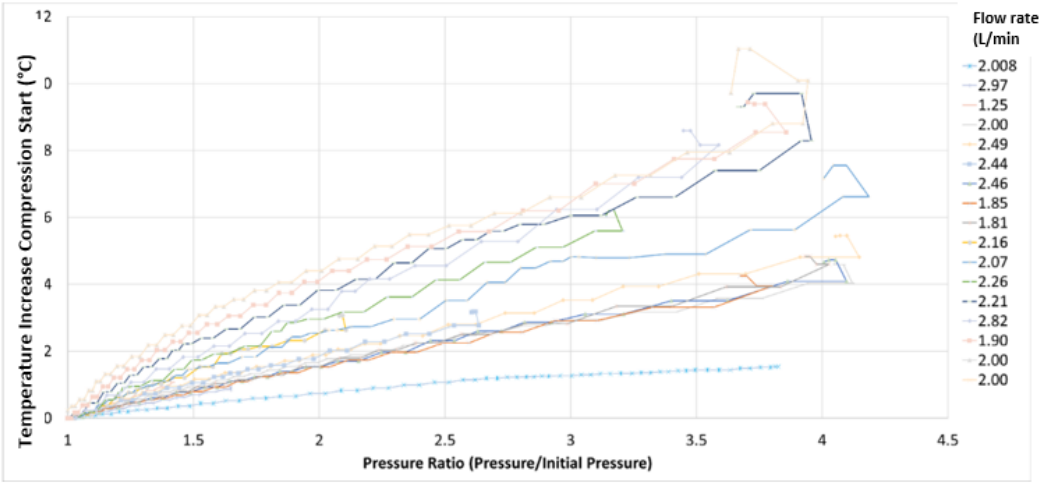

Figure 17. Temperature increase vs. pressure ratio for the single compression chamber.

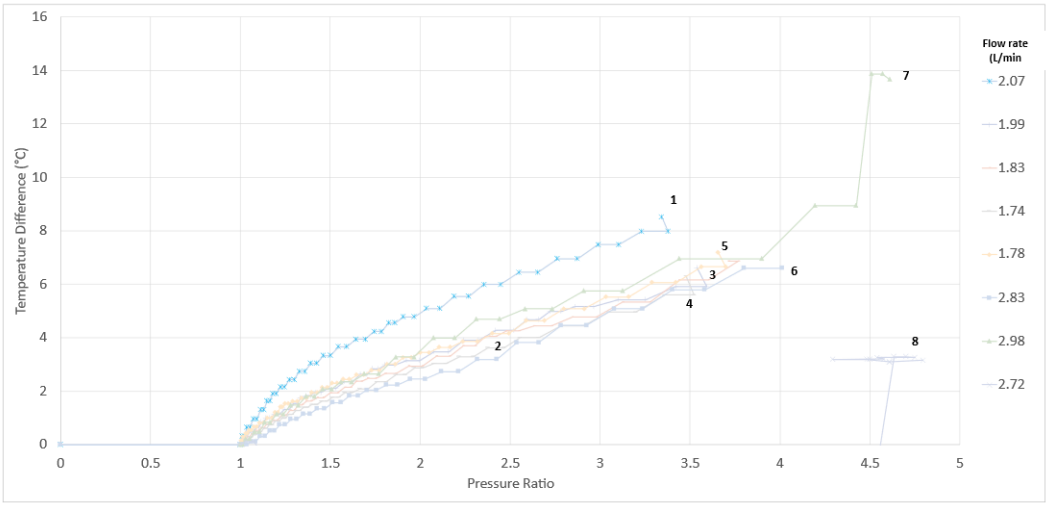

Figure 18. Eight compression cycles of the near-isothermal liquid compressor.

Finally, the same approximate flow rates were used in a second set of experiments, the results of which showed similar isothermal compression behavior over seven compression cycles; temperature difference vs. pressure ratio is plotted in Figure 19. Similar behavior was observed during cycles 1–3, but the temperature increased near the ends of cycles 4 and 5. Cycles 1–5 were at 2 L/min, and cycles 6 and 7 were at 3 L/min. The catch can filled on cycle 7. In the first compression cycle with the 3 L/min flow rate, no liquid was seen in the catch can. Thus, the issue appears to have occurred during the first liquid discharge of the faster (3 L/min) flow rate. This allowed a maximum cycle speed of 2–3 L/min for this first prototype. On the third

compression at this rate (cycle 8, the data from which are not shown in Figure 19), the catch can overfilled, and the experiment was stopped. The data obtained just before the catch can was filled were useful for the second-generation prototype's design and operation. In this period, the liquid temperature matched the CO_2 discharge temperature in the cycle just prior to the liquid entering the catch can. Therefore, when the two temperatures matched, it can be assumed that too much liquid was passing into the accumulator, a phenomenon that the team calls *carryover*.

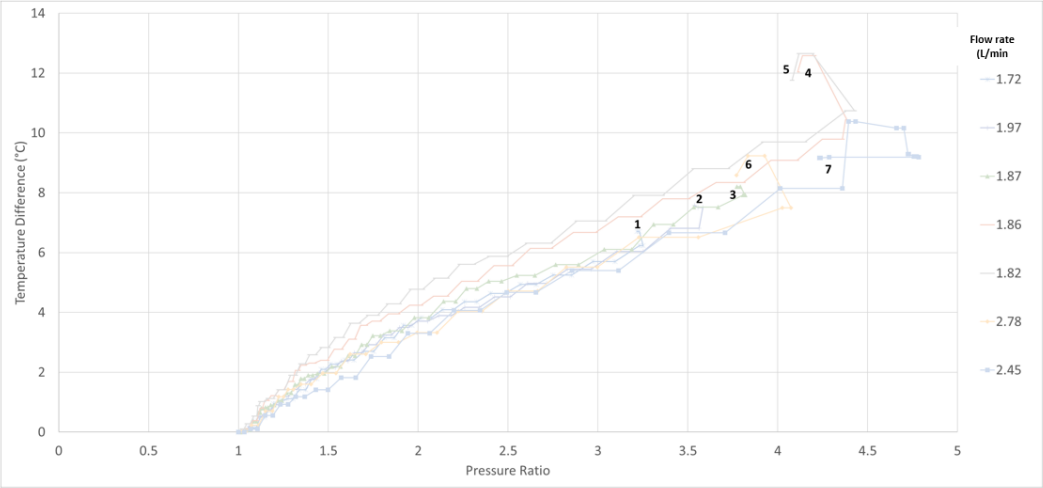

Figure 19. Seven compression cycles of the near-isothermal liquid compressor.

Carryover of the PG was not expected in these tests because the team observed mass flow rates and the level of PG in the compression chambers closely. However, the pump was manually operated for these tests. Therefore, the team suggests the following potential reasons for having observed carryover at unexpected times:

- The mass flow meter was not able to measure the total volume of liquid accurately at this compression rate.
- The level sensor was unable to indicate the level of the liquid accurately at this compression rate.
- The user was unable to actuate the totalizer and stop the pump with sufficient time.
- A previously unseen physical phenomenon occurred inside the chamber because of the increased speed (i.e., higher entrainment of CO_2 in the liquid caused the volume available for compression to decrease).

Observation of many bubbles in the sight glass of the catch can when it filled supports the last potential reason. Prior to testing at the increased flow rate, separation of the CO_2 and liquid was expected to require some time, which would have increased the likelihood of the reduction in available compression volume.

2.2 NOZZLE TESTING RESULTS

Because visualizing the flow characteristics of the spray of droplets in the single compression chamber was not possible, the team decided to use various nozzles to spray water into a clear plastic pipe to observe the spray pattern and simulate conditions in the compression chamber. It was not an exact simulation because the physical properties of water differ from those of PG. The discharge coefficient was used to determine the approximate flow rate when a differential pressure of 12 psi was applied to the nozzle. The entrainment of air was substantial with the nozzle used in the first prototype such that a forceful jet of spray droplets penetrated the surface of the water by several inches as shown in Figure 20. The team believes this caused foaming

of the PG, leading to spurious results on the liquid-level switch and therefore to challenges with manually operating valves to prevent carryover of the PG into the piping system leading to the catch can. The nozzle supplier suggested better designs for this application, and five additional nozzles were sourced to evaluate various spray patterns. The team selected the best option for the second prototype by observing which option created the finest spray to increase heat transfer and minimized the height of air-water mixing at the end of the compression cycle.

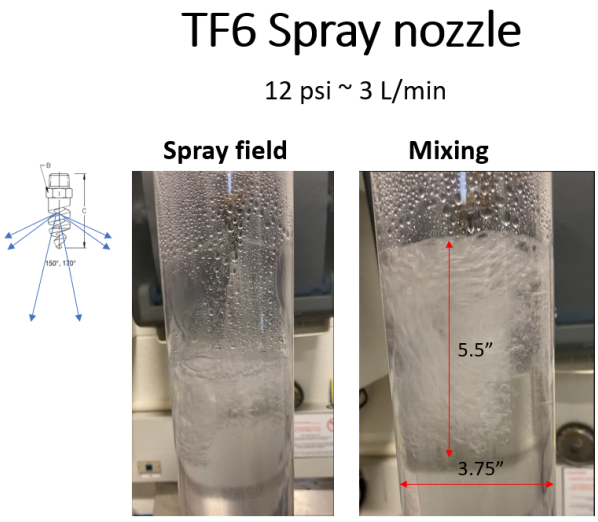

Figure 20. Spray visualization of the first nozzle used in the prototype.

An additional issue was noted regarding the nozzle used in the first prototype. The original design was a nozzle with a spiral cone that produced a full 150° cone of spray. Discussions with the nozzle supplier indicated that the desired liquid flow rates were slightly below the design flow rate range for this nozzle as specified by the manufacturer. This was further evidence that influenced the selection of different nozzles for the second prototype.

2.3 SECOND PROTOTYPE: TWO COMPRESSION CHAMBERS

The second prototype had two compression chambers to allow continuous automatic compression, meaning that while gas in one chamber was being compressed, gas in the other chamber was discharged. An accumulator in the system evened out fluctuations of the outlet pressure. The P&ID is shown in Figure 21. The second prototype improved on the design of the first prototype in three ways. First, the second prototype used two hydraulic cylinders and a system of solenoid valves to regulate the flow of compression fluid into the compression chambers. The hydraulic cylinders were rigidly mounted to a steel plate to enable finer control of the compression liquid and recovery of decompression energy. This improvement allowed the injection of only the desired amount of compression fluid into the chambers. The second improvement was the addition of a second level switch on the compression chambers. The previous prototype used only one level switch. The second level switch would allow programming of LabVIEW to fill the chambers with oil accurately without regard to the rate of filling. Faster filling rates would better simulate the flow rate of refrigerant that will be required in an actual heat pump. A solid model of a compression chamber is shown in Figure 22. The last improvement was the use of more appropriate nozzle designs with an appropriate design liquid flow rate range to reduce the chance of foaming, which was thought to lead to carryover. Photos of one of the chambers during fabrication are shown in Figure 23. The top (threaded portion) enabled the team to evaluate multiple nozzles by inserting different plug and nozzle combinations. This second prototype had a

reduced mass and reached steady state quicker than the first prototype to aid in modeling. This chamber also matched the computational fluid dynamics (CFD) design more accurately.

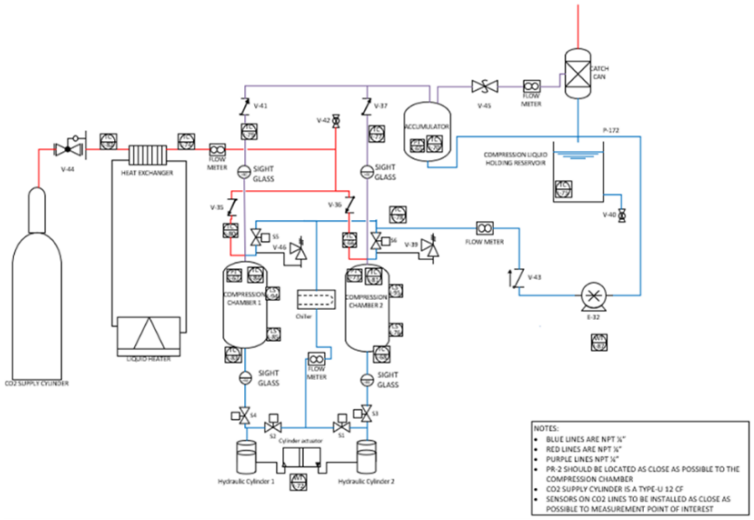

Figure 21. P&ID of the experimental facility of the second-generation isothermal liquid-piston compressor.

Figure 22. Compression chamber with two level switch locations. The locations of the level switches are labeled as N1 and N2.

Figure 23. Pictures of the first fabricated compression chamber.

Photos of the second prototype are shown in Figure 24 and Figure 25. Because 75% of the first prototype was used in the second prototype, building a table that connected to the existing table was the easiest path forward for construction.

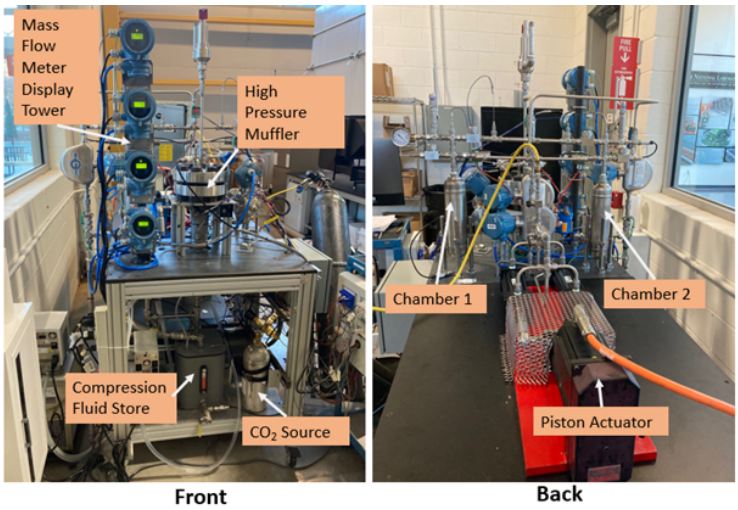

Figure 24. Photos of the front and back of the second prototype with major components labeled.

Figure 25. Photo of the side of the second prototype showing the DAQ computer.

Communication between the hydraulic piston actuator and the DAQ was very important because the timing of the actuator movements and solenoid positions were considered critical to proper operation. Two methods of establishing control of these devices in time were implemented: adding external position sensors to the actuator yoke and communicating to the actuator through Modbus on LabVIEW.

The system of solenoid valves added to control the flow of PG between the two compression chambers did not work as planned. Figure 26 describes the locations of the solenoids. Though they were specified to be able to operate with high pressure difference, during the initial CO_2 pressurization, the solenoids, specifically S7, allowed low-pressure gas through its internals when closed. The manufacturer's representative was contacted but did not supply a satisfactory resolution. The issue with the solenoids was unresolved. A manual valve was purchased to replace S7, but insufficient project funds meant that no further changes could be made. The result was that useful data were never obtained from the second prototype.

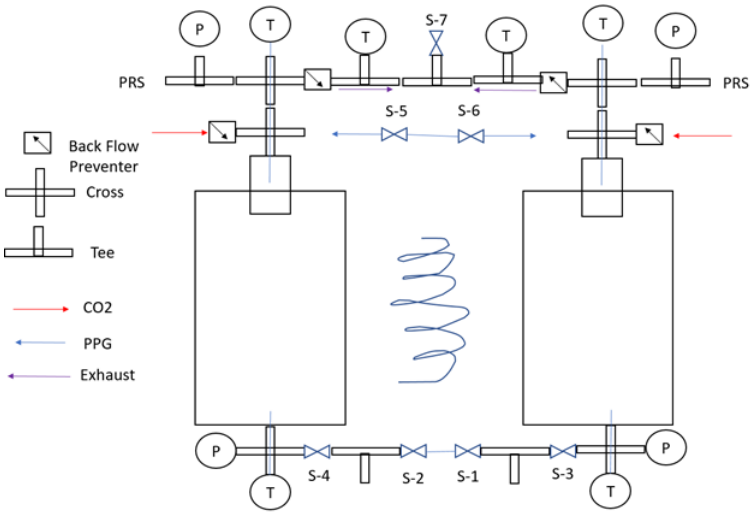

Figure 26. Chamber setup with control solenoid locations.

2.4 DISCUSSION OF PROTOTYPE DESIGN AND TESTING

After successful operation of the first prototype and unsuccessful operation of the second prototype, the team made several conclusions that could be useful in future experimental work on an isothermal LPC.

The relatively large thermal mass of the compression chamber affects the performance significantly during the initial cycles. Operation during the first cycles may also be affected by the required test conditions because of the heat lost to the ambient, which will be significantly different at test operating-temperature conditions than at the laboratory ambient temperature.

With the second prototype, troubleshooting the reasons for the poor results was difficult. The team could not accurately identify which valve was causing issues because the mass flow through each leg could not be observed. Therefore, it would be helpful if future prototypes were constructed with the ability for full mass and energy balance of each critical flow.

The instabilities at the fluid/gas interface were significant at PG flow rates of 3 L/min, causing significant carryover of liquid during decompression of the CO_2. These instabilities were not apparent at flow rates of 2 L/min for several cycles. This may suggest that in large chambers, compression speed is limited, at least with some nozzles.

With both prototypes, the team realized that the carryover of PG may be reduced or eliminated by changing the compression mode as the liquid piston rises to the top of the compression chamber. Though it may be difficult to program in LabVIEW, a potential solution is to change from liquid delivery through spray from the nozzle at the top of the chamber to liquid delivery at the bottom of the chamber while the compression stroke is completed.

Solenoid valves do not appear to work well in this application. Pneumatically controlled valves were suggested by the solenoid manufacturers. These may be more appropriate in future studies.

An ideal compression liquid would not allow CO_2 to dissolve easily. But liquids with this characteristic (e.g., mercury) are impractical to use. Carryover of the liquid and gas is likely in LPCs and will require carryover remediation techniques.

3. NUMERICAL STUDIES OF A LIQUID-PISTON COMPRESSOR

This section summarizes numerical studies of an LPC using CFD modeling approaches. First is a study of an LPC wherein liquid PG entered the compression chamber from the bottom inlet to create a liquid piston for compression. Second is a study in which PG liquid droplets were injected from the top to compress CO_2 gas in the chamber. Results from this work elucidate the entire cycle of compression and expansion in the liquid-piston design and will be used to improve the physics-based thermodynamic model used for the system design and evaluation of near-isothermal compression.

Figure 27 shows the configuration of the LPC considered in the first study. As in the previously described experimental work, the compression chamber could be filled from the bottom inlet nozzle or from the top spray nozzle. The compressor had a total height of 323.6 mm and comprised a cylindrical chamber with a vertical length of H_1 = 275.34 mm and an internal diameter of D_1 = 88.9 mm. The inlet nozzle had an internal diameter of D_2 = 19.05 mm. In Figure 27, the x- and z-coordinates represent the horizontal planes, and the y-coordinate denotes the vertical direction. The origin of the coordinate system is the center of the chamber at a distance of H_2 = 48.26 mm from the nozzle inlet. The compression chamber was designed to allow CO_2 to enter from the top and the compression fluid (i.e., liquid PG) to enter from the nozzle inlet at the bottom or from the spray nozzle at the top.

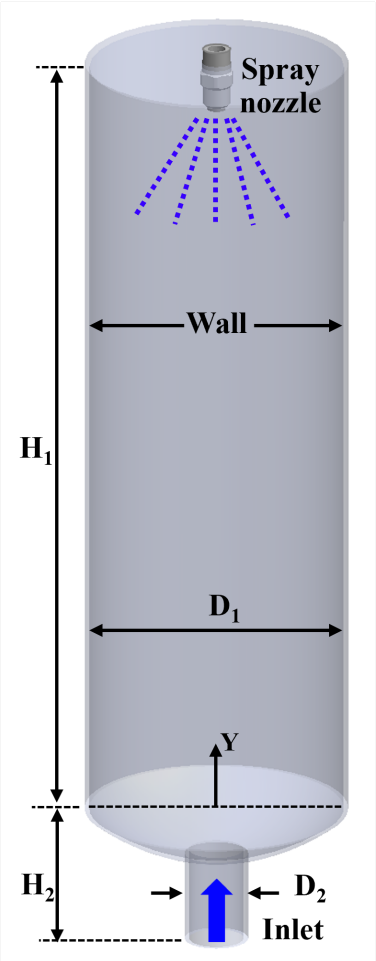

Figure 27. Design of the liquid-piston compressor considered in this study.

3.1 NUMERICAL SIMULATION OF AN LPC WITH BOTTOM INJECTION

This section presents numerical studies of an LPC in which the chamber filled with liquid PG from the bottom inlet to compress CO_2. Numerical simulations were performed using LES coupled with the multiphase volume of fluid (VOF) model to simulate the transient interface between liquid PG and CO_2 gas and to capture the heat and mass transfer within the volume of the compression chamber. In the present work, the wall-adapting local eddy-viscosity (WALE) subgrid scale (SGS) model featuring a novel form of the velocity gradient tensor in its formulation was applied because of its advantages over the Smagorinsky model. In a previous study of an LPC (Gouda et al. 2022), the performances of LES Smagorinsky and WALE subgrid models were compared, and the WALE model managed the flow transition and more accurately captured the near-wall region. The VOF model was selected because it is suitable for model flows involving immiscible fluids, fluid mixtures, free surfaces, and phase contact on numerical grids capable of resolving the interface between the phases (Muzaferija 1998). The VOF model is suitable for model flows involving immiscible fluids, fluid mixtures, free surfaces, and phase contact on numerical grids capable of resolving the interface between the phases. The team investigated the effects of boundary conditions applied to the CFD-VOF calculations (i.e., no wall, an adiabatic wall, and a thick wall with a heat flux subscribed) on the overall pressure and temperature as well as the transient evolutions of flow and heat transfer within the compression chamber, and the results are discussed in the following sections.

3.1.1 Computational Domain

In the studied configuration shown in Figure 28 (left), the internal volume of the chamber was initially occupied by CO_2 gas. The compression process started when liquid PG was injected into the chamber bottom via the nozzle inlet with a volume flow rate of $Q_1 = 2$ L/min and stopped when the chamber's internal pressure reached 8.6 MPa. The initial conditions of the chamber were a temperature of 305 K, a pressure of 2 MPa, and the liquid PG level at the origin $y = 0$. To reduce the computational cost, the numerical domain of the compression chamber was reproduced with a 45° angle portion with two cutting surfaces that were considered as symmetry planes as shown in Figure 28 (right). The thermal fluid flow phenomena within the chamber volume during the compression process were expected to be complex, involving unsteady compressible multiphase flow physics of liquid and gas associated with conjugated heat transfer. During the compression process, liquid PG was injected into the chamber at a constant volume flow rate such that the liquid velocity could be considered a constant. The CO_2 gas within the chamber volume was compressed, making the gas flow patterns dynamically evolve and become very complex. The CO_2 gas temperature during the compression increases, inducing heat transfer between the gas and liquid at their interface. Furthermore, convection heat transfer occurs among the gas, liquid, and chamber wall, depending on the spatial location of the gas–liquid interface, the gas flow patterns, the thermal resistance of the wall, and the ambient temperature. The chamber wall was specified by a no-slip boundary. In this study, numerical calculations were performed considering several boundary conditions of the chamber wall, including no wall (only the interior volume of the chamber), a wall with a constant temperature, and a wall with a constant heat flux. These considerations allowed for investigating the interactions between the solid wall and the flow inside the chamber during the compression process.

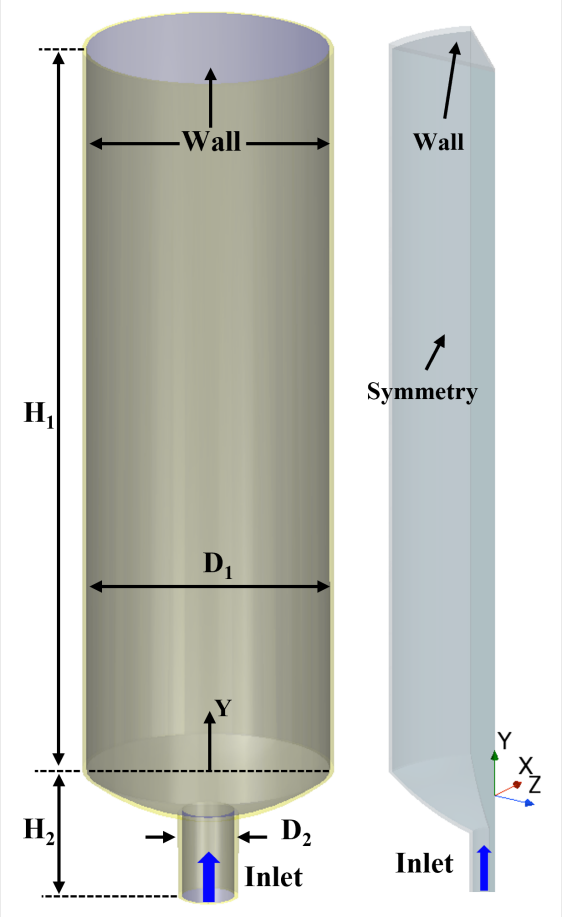

Figure 28. Design of the LPC (left) and the computational domain used in the numerical study of the LPC with a bottom injection (right).

3.1.2 Numerical Modeling

Applying the considerations suggested in previous studies (Gouda et al. 2021; Gouda et al. 2022), the following assumptions were made in the numerical modeling of the LPC in this study. The ideal gas law was applied for the gas phase (CO_2) with a specific heat of $C_p = 1,020.6$ J/kg·K, a thermal conductivity of $\lambda_g = 0.018153$ W/m·K, and a molecular weight of 44.01 kg/kmol. The Sutherland equation (shown in Equation 1) was applied for the temperature-dependent viscosity of CO_2:

$$\mu(T) = \mu \frac{T_0 + C}{T + C} \left(\frac{T}{T_0} \right)^{3/2}, \tag{1}$$

where the Sutherland coefficient $C = 110.4$, the reference temperature $T_0 = 273.15$ K, and the reference viscosity $\mu_0 = 1.716 \times 10^{-5}$ Pa·s. The liquid phase (PG) was considered incompressible flow with a density of $\rho_l = 1,048$ kg/m^3, a dynamic viscosity of $\mu_l = 0.056$ Pa·s, a specific heat of $C_p = 3,251$ J/kg·K, a thermal conductivity of $\lambda_g = 0.223$ W/m·K, and a molecular weight of 76.1 kg/kmol. No phase change occurred for the working fluids, and no mass transfer occurred between the liquid and gas phases.

The turbulent fluid motion is governed by conservation of mass, linear momentum, and energy, The first two are described by Equations 2 and 3, respectively, as follows:

$$\frac{\partial \rho}{\partial t} + \nabla \cdot (\rho \boldsymbol{v}) = 0, \tag{2}$$

where ρ is the density, and v is the continuum velocity.

$$\frac{\partial(\rho \boldsymbol{v})}{\partial t} + \nabla \cdot (\rho \boldsymbol{v} \otimes \boldsymbol{v}) = -\nabla \cdot (p\boldsymbol{I}) + \nabla \cdot \boldsymbol{T} + \boldsymbol{f}_b, \tag{3}$$

where $\otimes$ denotes the outer product, f_b is the resultant of the body forces per unit volume acting on the continuum, and σ is the stress tensor. For a fluid, the stress tensor is often written as the sum of normal stresses and shear stresses, $\sigma = -p\boldsymbol{I} + \boldsymbol{T}$, where $\boldsymbol{I}$ is the identity matrix, p is the pressure and $\boldsymbol{T}$ is the viscous stress tensor.

Conservation of energy is described by Equation 4.

$$\frac{\partial(\rho E)}{\partial t} + \nabla \cdot (\rho E \boldsymbol{v}) = \boldsymbol{f}_b \cdot \boldsymbol{v} + \nabla \cdot (\boldsymbol{v} \cdot \boldsymbol{\sigma}) - \nabla \cdot \boldsymbol{q} + \boldsymbol{S}_E, \tag{4}$$

where E is the total energy per unit mass, q is the heat flux, and S_E is an energy source per unit volume. An LES resolves turbulent structures in space everywhere in the flow domain down to the grid limit, whereas subgrid models approximate the effect of the subgrid structures on the flow field. To resolve the crucial turbulent structures near the wall, this approach requires an excessively high mesh resolution in the wall boundary layer—not only in the direction normal to the wall but also in the flow direction. LES is an inherently transient technique in which the large scales of the turbulence depend on the geometry and are directly resolved everywhere in the flow domain, whereas the small-scale motions (eddies) behave universally and are modeled (Smagorinsky 1963). The large-scale motions are resolved by the filtered Navier–Stokes equation, and the small-scale motions are modeled by SGS models. The governing equations for LES are derived by spatially filtering the time-dependent 3D Navier–Stokes equations. Each solution variable ϕ is decomposed into a filtered value, $\tilde{\phi}$, and a subfiltered, or subgrid, value, ϕ', as follows:

$$\phi = \tilde{\phi} + \phi', \tag{5}$$

where ϕ represents velocity components, pressure, energy, or species concentration. The spatial filtering removes the smaller eddies—which are associated with higher frequencies—and thereby reduces the range of scales that must be resolved. LES filtering can be explicit or implicit. Explicit filtering applies a filter function (such as box or Gaussian) to the discretized Navier–Stokes equations. The filtering of the generic instantaneous flow variable, $\phi(t, x)$, is defined as follows:

$$\tilde{\phi}(t, x) = \iiint_{-\infty}^{\infty} G(x - x', \Delta)\phi(t, x')dx', \tag{6}$$

where $G(x, \Delta)$ is the filter function characterized by a filter width $\Delta = \left(\Delta_x \Delta_y \Delta_z\right)^{1/3}$. For this approach, the computational grid determines the scales of the eddies that are filtered out. Inserting the decomposed solution variables into the Navier–Stokes equations yields equations for the filtered quantities of mass, momentum, and energy transport that can be expressed as follows:

$$\frac{\partial \rho}{\partial t} + \nabla \cdot (\rho \tilde{\boldsymbol{v}}) = 0, \tag{7}$$

$$\frac{\partial}{\partial t}(\rho \tilde{\boldsymbol{v}}) + \nabla \cdot (\rho \tilde{\boldsymbol{v}} \otimes \tilde{\boldsymbol{v}}) = -\nabla \cdot (\tilde{p}I) + \nabla \cdot \left(\tilde{\boldsymbol{T}} + \boldsymbol{T}_{SGS}\right) + \boldsymbol{f}_b, \tag{8}$$

$$\frac{\partial}{\partial t}\left(\rho \tilde{E}\right) + \nabla \cdot (\rho \tilde{E} \tilde{\boldsymbol{v}}) = -\nabla \cdot \tilde{p}\tilde{\boldsymbol{v}} + \nabla \cdot \left(\tilde{\boldsymbol{T}} + \boldsymbol{T}_{SGS}\right)\tilde{\boldsymbol{v}} - \nabla \cdot \tilde{\boldsymbol{q}} + \boldsymbol{f}_b \tilde{\boldsymbol{v}}, \tag{9}$$

where $\tilde{\boldsymbol{v}}$ is the filtered velocity, $\tilde{p}$ is the filtered pressure, $\boldsymbol{I}$ is the identity tensor, $\tilde{\boldsymbol{T}}$ is the filtered stress tensor, $\tilde{E}$ is the filtered total energy per unit mass, and $\tilde{\boldsymbol{q}}$ is the filtered heat flux. These stresses result from the interaction between the larger resolved eddies and the smaller unresolved eddies and are modeled using the Boussinesq approximation as follows:

$$\boldsymbol{T}_{SGS} = 2\mu_t \boldsymbol{S} - \frac{2}{3}\left(\mu_t \nabla \cdot \tilde{\boldsymbol{v}}\right)\boldsymbol{I}, \tag{10}$$

where $\boldsymbol{S}$ is the strain rate tensor and is computed from the resolved velocity field $\tilde{\boldsymbol{v}}$. The mean strain rate tensor $\boldsymbol{S}$ is given by

$$\boldsymbol{S} = \frac{1}{2}\left(\nabla \bar{\boldsymbol{v}} + \nabla \bar{\boldsymbol{v}}^T\right), \tag{11}$$

where $\boldsymbol{v}$ is the mean velocity. The SGS turbulent viscosity, μ_t, must be described by an SGS model that accounts for the effects of small eddies on the resolved flow. The WALE SGS model employed in this study (Nicoud and Ducros 1999) provides the following mixing-length-type formula for the SGS viscosity:

$$\mu_t = \rho \triangle^2 S_w, \tag{12}$$

where $\triangle$ is the length scale or grid filter width and S_w is a deformation parameter. The length scale $\triangle$ is defined in terms of the cell volume, V:

$$\triangle = \frac{C_w V^{1/3}}{min\left(\kappa d, C_w V^{1/3}\right)}, \tag{13}$$

where C_w is a model coefficient and κ is the von Karman constant. The deformation parameter, S_w, is defined as follows:

$$S_w = \frac{\boldsymbol{S}_d : \boldsymbol{S}_d^{3/2}}{\boldsymbol{S}_d : \boldsymbol{S}_d^{5/4} + \boldsymbol{S} : \boldsymbol{S}^{5/2}}. \tag{14}$$

The tensor, $\boldsymbol{S}_d$, is defined as follows:

$$\boldsymbol{S}_d = \frac{1}{2}\left[\nabla \boldsymbol{v} \cdot \nabla \boldsymbol{v} + (\nabla \boldsymbol{v} \cdot \nabla \boldsymbol{v})^T\right] - \frac{1}{3} tr\left(\nabla \boldsymbol{v} \cdot \nabla \boldsymbol{v}\right)\boldsymbol{I}. \tag{15}$$

For LES models, the definition of the filtered heat flux, $\tilde{\boldsymbol{q}}$, in the energy equation is based on a Boussinesq approximation, where the heat flux is assumed to be proportional to the SGS viscosity and is defined as follows:

$$\tilde{\boldsymbol{q}} = -\left(\lambda_g + \frac{\mu_t C_p}{Pr_t}\right)\nabla \tilde{T}, \tag{16}$$

where λ_g is the fluid thermal conductivity, μ_t is the SGS viscosity as given by the respective SGS model, C_p is the specific heat, Pr_t is the turbulent Prandtl number, and $\tilde{T}$ is the filtered temperature.

The VOF multiphase model (Hirt and Nichols 1981) was chosen to simulate and identify the interface between gas and liquid. Because of its numerical efficiency, the VOF model is suited for simulations of flows wherein each phase constitutes a large structure with a relatively small total contact area between phases (Siemens 2021). In the VOF model, volume fraction is defined as the spatial distribution of each phase at a given time. It is calculated by solving a transport equation for the phase volume fraction, which is implemented in the STAR-CCM+ segregated flow model (Siemens 2021). To ensure simulation stability, the Courant–Friedrichs–Lewy (CFL) number at the liquid–gas interface should be limited to 1, and better results with a sharp resolution of the two phases are obtained with a CFL number around 0.5 (Connell and Cashman 2016). In this study, a second-order convection scheme implemented in the high-resolution

interface-capturing options was used throughout all simulations to capture sharp interfaces between the two phases accurately, namely air and water. The calculations were performed under the transient state using implicit schemes, and the Semi-Implicit Method for Pressure-Linked Equations (SIMPLE) algorithm was applied for the pressure–velocity coupling. The calculation time step dt was 0.001 s to keep the CFL number less than 0.5. According to the STAR-CCM+ manuals (Siemens 2021), the use of implicit schemes and the SIMPLE algorithm facilitates good results with higher time steps even with very high Courant numbers in VOF simulations.

3.1.3 Domain Discretization

Computational meshes were generated using polyhedral and prismal layer-meshing operations. Mesh generation was performed using the automatic meshing capabilities in STAR-CCM+: the surface remesher, polyhedral mesher, and prism layer mesher. The surface remesher performed surface vertex retessellation of the imported 3D CAD to optimize surface faces based on the target edge length and proximity refinements. The polyhedral mesher used an arbitrary polyhedral cell shape to build the core mesh. In the polyhedral mesher process, a tetrahedral mesh was first generated for the input surface. Second, a dualization scheme was used to create the polyhedral mesh from the underlying tetrahedral mesh. The volume growth rate controlled how quickly the cell size increased with increasing distance from the surface and from refinement zones to mesh away from the zones. The maximum cell size control restricted how large cells could grow. The prism layer mesher generated a subsurface to extrude a set of prismatic cells from region surfaces into the core mesh. This layer of cells was necessary to improve the accuracy of the flow solution. Figure 29 illustrates the computational domain with two vertical planes, XZ_0 and midplane XZ_3 (i.e., side surfaces); a midplane, XZ_2; and a horizontal plane, Y_1. The computational mesh generated in the plane XZ_1, the midplane XZ_2, and the plane Y_1 is also shown. The sensitivity of the mesh discretization on relevant fluid-flow and heat-transfer quantities was investigated. Coarse, medium, and fine meshes were generated using a base cell size of 0.1905 mm with refinements to the cell sizes in the core flow and wall layers, such as target surface sizes, surface and volume grow rates, and numbers of prism layers. The resulting numbers of cells, including both fluid and solid parts, were 7.1×10^6 for the coarse mesh, 10.9×10^6 for the medium mesh, and 18.8×10^6 for the fine mesh. The numbers of fluid cells were 3.7×10^6 for the coarse mesh, 5.6×10^6 for the medium mesh, and 8.7×10^6 for the fine mesh. Mesh sensitivity was evaluated by comparing the temporal evolution of quantities of interest such as volume-averaged temperature of CO_2, volume-averaged pressure of CO_2, and volume-averaged velocity of CO_2. To reduce the computational effort required for the mesh sensitivity study, numerical calculations using the coarse, medium, and fine meshes were performed for 8 s when the CO_2 pressure increased from 2 to 2.5 MPa. Figure 30 compares the volume-averaged temperatures and velocities of CO_2 gas inside the chamber during the 8 s compression process obtained using the coarse, medium, and fine meshes. The results obtained using the medium mesh (10.9×10^6 cells) and the fine mesh (18.8×10^6 cells) were similar. However, the computational time of the fine mesh was considerably longer than those of the coarse and medium meshes. Therefore, the medium mesh and corresponding meshing methodology were selected for the numerical investigations of the LPC.

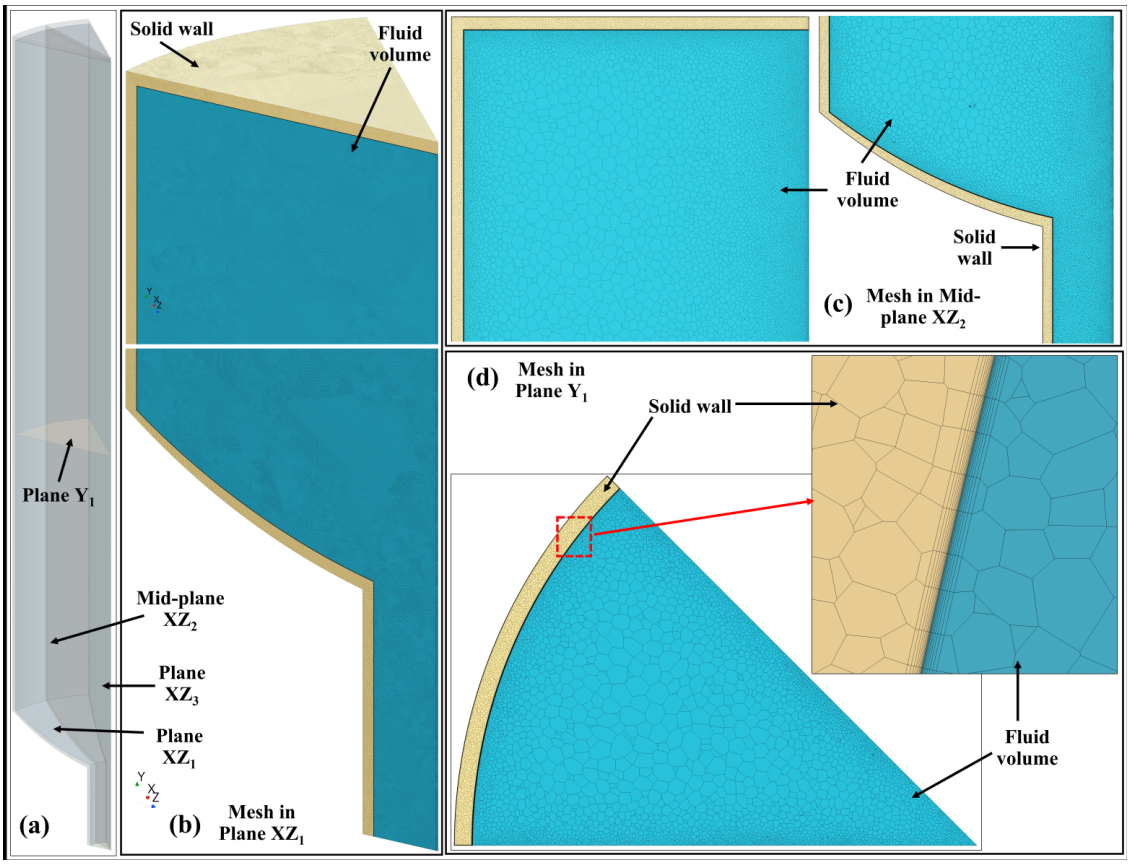

Figure 29. (a) Computational domain with vertical plane XZ_0, vertical midplanes XZ_2 and XZ_3, and horizontal plane Y_1. Computational mesh generated in the solid wall (yellow) and fluid region (blue) used in this study: (b) mesh in plane XZ_1, (c) mesh in midplane XZ_2, and (d) mesh in plane Y_1.

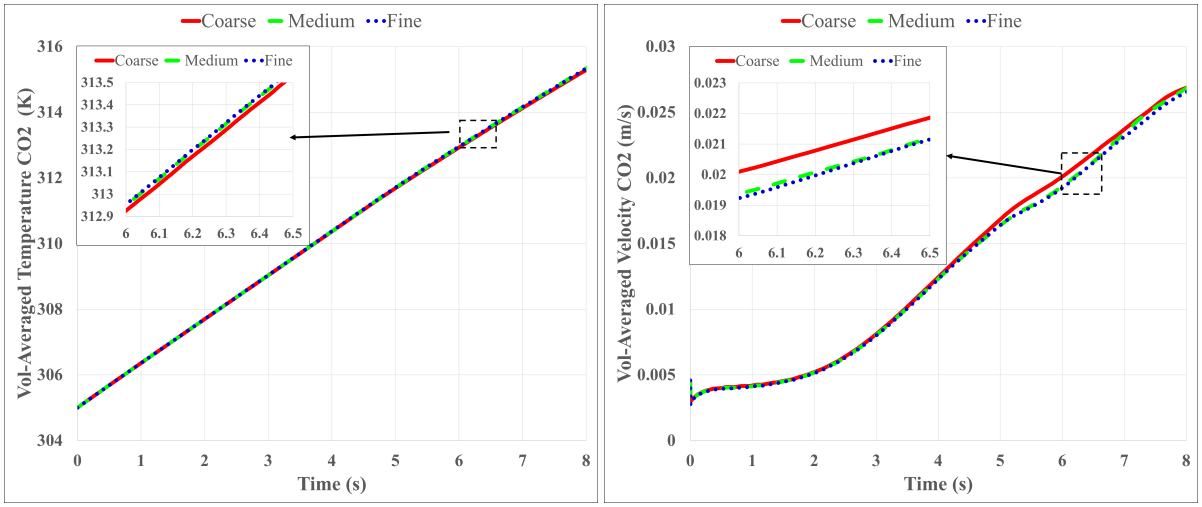

Figure 30. Comparison of volume-averaged transient temperatures and velocities of CO_2 gas inside the chamber during the 8 s compression process obtained using coarse, medium, and fine meshes.

3.1.4 Results and Discussion

3.1.4.1 Effects of modeling conjugate heat transfer with fluid–solid wall interactions

This subsection describes the conjugate heat transfer simulations that were performed on the numerical domain with various boundary conditions applied: no wall (only the fluid volume considered), a wall with a constant temperature of 305 K, and a wall with a constant heat flux of 60 W/m^2. Results obtained from the calculations are compared to study the effects of the chamber wall on the flow and heat transfer within the chamber during the compression process.

Figure 31 shows the temporal evolution of the volume-averaged pressures, temperatures, and velocities of CO_2 in the compression chamber obtained from the LES calculations of a liquid-piston domain corresponding to the boundary conditions of no wall, a wall with a constant temperature, and a wall with a constant heat flux. Figure 31(a) shows the CO_2 gas pressure within the chamber from the beginning (i.e., when liquid PG was injected into the chamber using the bottom nozzle inlet) to the end of the compression process (i.e., when the internal CO_2 pressure reached 8.58 MPa). The LES calculation with no wall had its maximum pressure of 8.58 MPa at t = 34.1 s, whereas the LES calculations with a constant wall temperature and with a constant wall heat flux reached 8.58 MPa at t = 35.5 s. Figure 31(b) shows that the volume-averaged temperatures of CO_2 within the compression chamber obtained from the LES calculation with no wall increased from 305 to 392.7 K, whereas the peak CO_2 temperatures were 354.9 and 355.15 K for the LES calculations with constant wall temperature and with constant wall heat flux, respectively. The evolution of CO_2 temperatures during the compression process was similar: a maximum temperature difference of 1.6 K occurred when the chamber wall was considered in the numerical simulations that applied the isothermal or heat flux condition. However, the LES calculations with no wall resulted in a CO_2 temperature that deviated from other calculated temperatures at 3.4 s: the temperature difference was 0.1 K, and the maximum temperature was 37.4 K. Comparison of volume-averaged velocities of CO_2 gas within the chamber during the compression process clearly indicates the differences of gas kinetics when the presence of a chamber wall was considered in the LES calculations. Without considering the wall, the averaged CO_2 gas velocity was between 2.6×10^{-3} and 3×10^{-3} m/s and remained stable during the compression. On the other hand, when the effects of the chamber wall were considered in the conjugate heat transfer calculations, the averaged CO_2 gas velocity increased from approximately 3×10^{-3} m/s at the beginning to its peak of 3×10^{-2} m/s at 11.4 s and then gradually reduced to 2.1×10^{-2} m/s when the compression process finished.

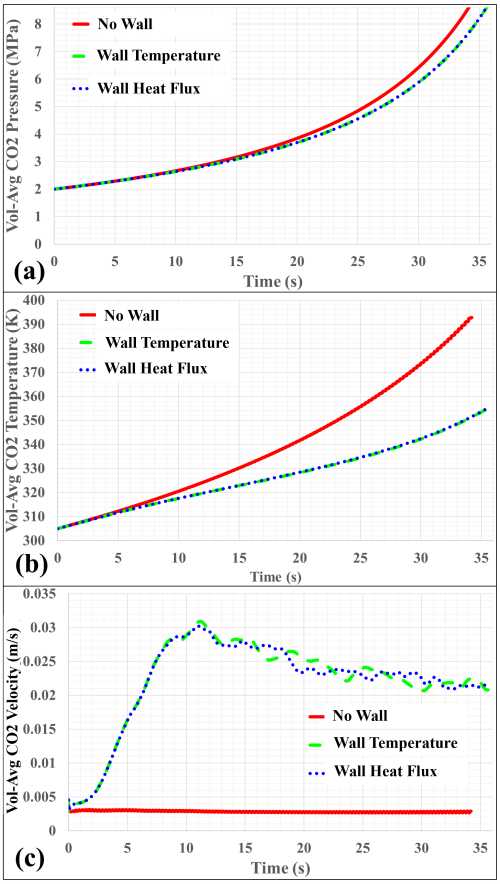

Figure 31. Comparisons of volume-averaged (Vol-Avg) CO_2 (a) pressures, (b) temperatures, and (c) velocities obtained from the simulations using boundary conditions of no wall, a wall with a constant wall temperature, and a wall with a constant heat flux.

Figures 32 and 33 show the color contours of CO_2 temperature and velocity magnitudes, respectively, at the instant of $t = 20$ s obtained from the LES calculations using no wall, a wall with a constant temperature, and a wall with a constant heat flux. Figure 32(a) and Figure 33(a) show that, when the chamber wall was excluded from the calculation, the flow and heat transfer behaviors inside the volume of the compression chamber were stable. At the instant when $t = 20$ s, the injection of liquid PG into the domain through the bottom nozzle inlet only slightly affected the liquid–gas interface because of the large liquid depth. In the CO_2 gas volume, the temperature was distributed uniformly in the radial direction whereas it increases almost linearly in the vertical direction, except in a small region near the gas–liquid interface where a large temperature gradient was observed, and no dynamic flow patterns were observed. On the contrary, Figure 32(b) and (c) and Figure 33(b) and (c) depict dynamic and complex patterns of CO_2 temperature and velocity fields in the chamber obtained from the LES calculations using the constant wall temperature and constant wall heat flux. These temperature and velocity contours at the instant of $t = 20$ s are not the same. However, they reveal similar small- and large-scale flow and temperature patterns. Overall, the temperature fields in the gas volume displayed an increase of temperature from the gas–liquid interface to the top wall of the compression chamber. Near the chamber wall, heat transfer between the cold wall and hot CO_2 gas was indicated by the presence of a gas layer. This thin gas layer was colder than the gas in the central region, creating an internal density-driven flow region where cold (heavy) gas near the wall moved downward and hot (light) gas in the center rose upward.

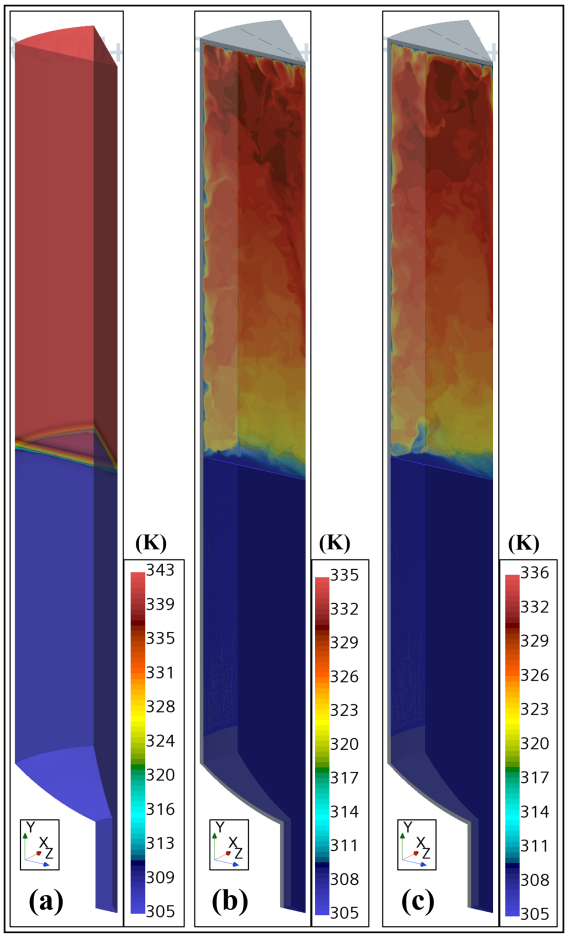

Figure 32. Color contours of CO_2 temperature at t = 20 s obtained from the LES calculations using boundary conditions of (a) no wall, (b) a wall with a constant temperature, and (c) a wall with a constant heat flux.

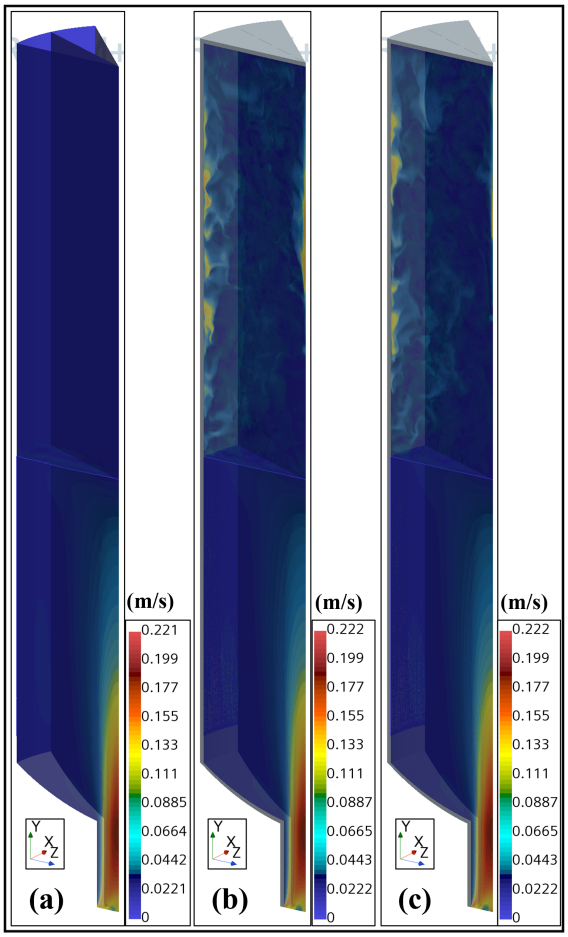

Figure 33. Color contours of CO_2 velocity magnitude at the instant of t = 20 s obtained from the LES calculations using boundary conditions of (a) no wall, (b) a wall with a constant temperature, and (c) a wall with a constant heat flux.

Comparisons of volume-averaged pressure, temperature, and velocity with instantaneous contours of the temperature and velocity of CO_2 gas within the chamber during the compression process highlight the importance and relevance of modeling the chamber wall in the simulations of an LPC. Therefore, the results presented in the next subsection were obtained from the LES calculations using a constant wall heat flux.

3.1.4.2 Results of an LES calculation with a constant wall heat flux condition

This subsection presents the flow and temperature fields obtained from an LES calculation of an LPC with liquid PG injected from the chamber's bottom nozzle inlet at a volume flow rate of Q_1 = 2 L/min. The chamber was initially occupied by CO_2 gas, and the initial conditions of the chamber were a temperature of 305 K and a pressure of 2 MPa. The compression process stopped when the internal pressure of the chamber reached 8.6 MPa. The averaged temperature of CO_2 gas within the chamber was an important indicator of the studied LPC's progress through the compression process. In this study, the temperature of the CO_2 gas increased from T_0 = 305 K (t = 0 s) to T_{max} = 355.15 K (t_{max} = 35.5 s). This temperature increase is approximately 16% and far smaller than the value of 28.7% for the adiabatic case (T_{max} = 392.7 K); therefore, the compression could be considered as near isothermal. In a study of an LPC using air and water (Gouda et al. 2021; Gouda et al. 2022), the authors reported temperature increases of 11.1% and

79% for near-isothermal and adiabatic cases, respectively. The evolution of CO_2 gas temperature shown in Figure 31(b) depicts different stages of the compression process:

- Stage 1, from t = 0 to 4.3 s: the temperature of CO_2 gas increased almost linearly by about 1.35 K/s.
- Stage 2, from t = 4.3 to 24.9 s: the temperature of CO_2 gas increased more slowly, by about 1.17 K/s.
- Stage 3, from t = 24.9 to 35.5 s: the temperature of CO_2 gas increased rapidly from 1.4 to 2.6 K toward the end of the compression. The temperature curve in this stage had a convex (parabolic) shape.

Different stages in the compression process of an LPC correspond to different flow and heat transfer regimes within the chamber. Figures 34 and 35 and Figures 36 and 37 illustrate the temperature and velocity fields, respectively, that evolved within the chamber during the compression process at several instances ranging from 0.7 to 35.5 s. The compression started when PG liquid was injected into the chamber through the inlet nozzle at the bottom. Because the level of liquid PG increased, the temperature of CO_2 gas within the top volume started to increase. In stage 1, the interface between the CO_2 gas and PG liquid was influenced, and surface waves were created: a peak occurred at the center of the chamber volume. The interface fluctuation induced a movement of CO_2 gas volume near the interface toward the chamber vertical wall. This movement initiated the heat transfer between the gas and liquid at the interface, between the gas and solid wall, and induced the mixing phenomena within the gas volume. (Figures 34 and 36 show temperature and velocity fields for t = 0.7 to 4.3 s.) At the end of stage 1 and transitioning into stage 2, thin layers of colder CO_2 formed along the vertical and top walls because of the heat transfer between the solid wall and CO_2 gas. Colder gas, which is denser, was found to either move downward along the vertical wall or fall into the gas from the top wall. The thin gas layers further exchanged heat while moving along the vertical wall, expanded in width, and accelerated until it impinged upon the liquid surface. After the impingement at the interface near the vertical wall, the CO_2 gas diverged back into the gas volume and strongly enhanced the flow and heat transfer mixing inside the central gas region. The combination of these dynamic flow movements established a large circulation flow pattern within the chamber volume in which the colder CO_2 gas layer moved downward along the side wall and the warmer CO_2 gas volume moved upward in the central region. The color contours of temperature and velocity fields of t = 5.7 to 25 s in Figures 35 and 37 reveal that highly dynamic flow patterns evolved within the chamber, particularly after t = 10 s, such that the gas mixing occurred within the entire internal volume of CO_2 gas. Furthermore, a temperature gradient was observed: a colder region was near the gas–liquid interface, and a warmer region was located at the top of the chamber. In stage 3, as the liquid level increased—significantly compressing the gas and increasing pressure and temperature within the CO_2 gas volume—the gas temperature increased rapidly. This behavior could be explained by the reduction of heat transfer surface between the solid wall and gas layer as well as the gas volume at the top of the chamber.

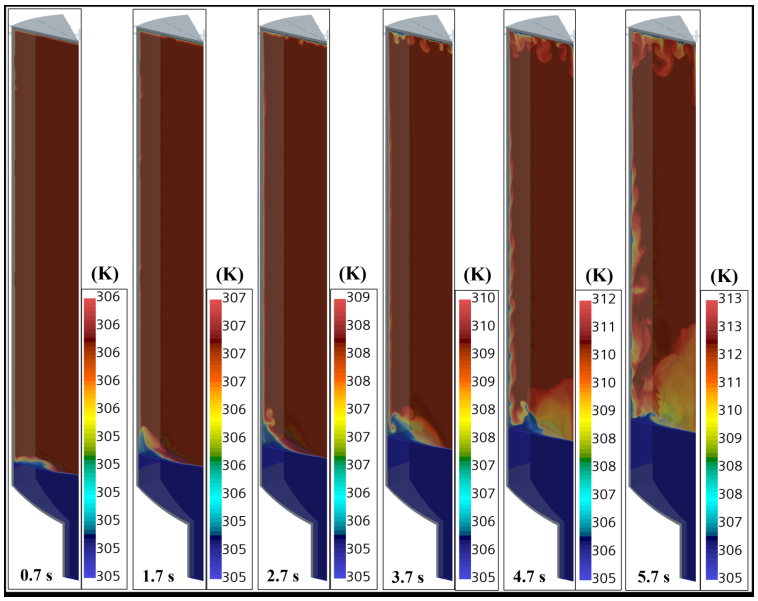

Figure 34. Temperature contours of CO_2 and PG within the chamber at t = 0.7, 1.7, 2.7, 3.7, 4.7, and 5.7 s. Results were obtained from the LES calculation of the compression process using a constant wall heat flux condition.

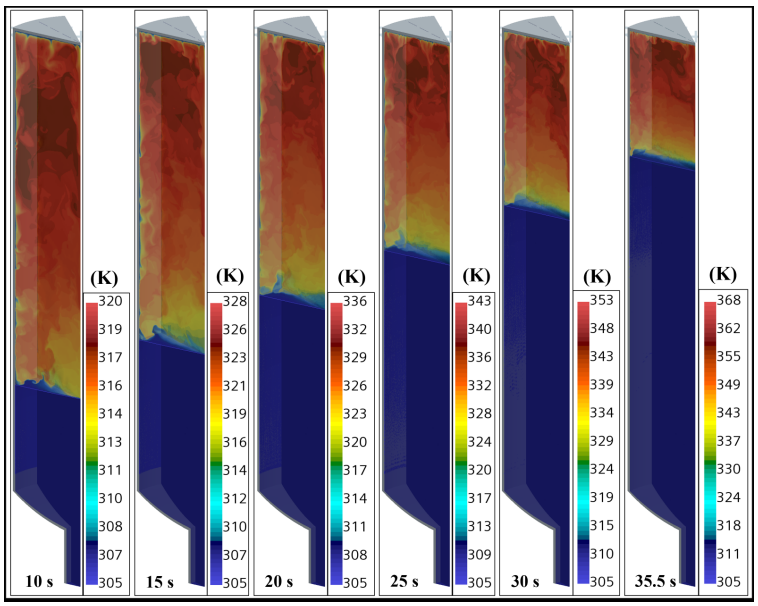

Figure 35. Temperature contours of CO_2 and PG within the chamber at t = 10, 15, 20, 25, 30, and 35.5 s. Results were obtained from the LES calculation of the compression process using a constant wall heat flux condition.

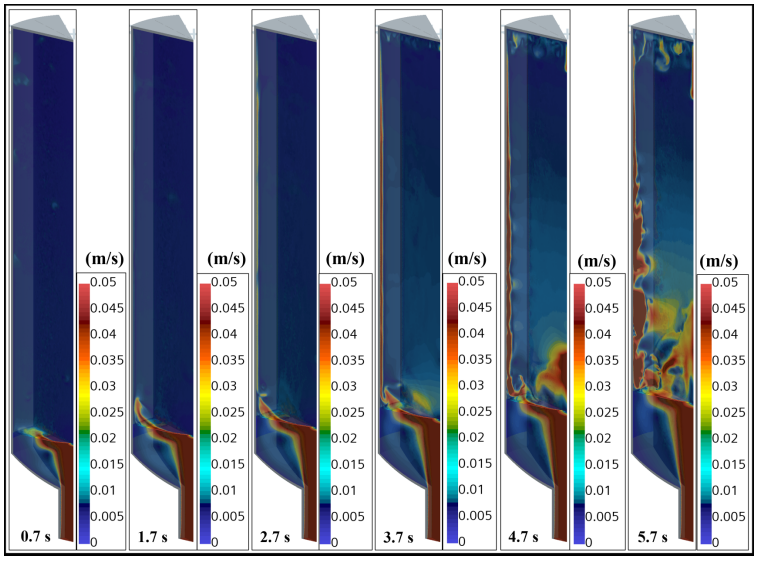

Figure 36. Velocity magnitude contours of CO_2 and PG within the chamber at t = 0.7, 1.7, 2.7, 3.7, 4.7, and 5.7 s. Results were obtained from the LES calculation of the compression process using a constant wall heat flux condition.

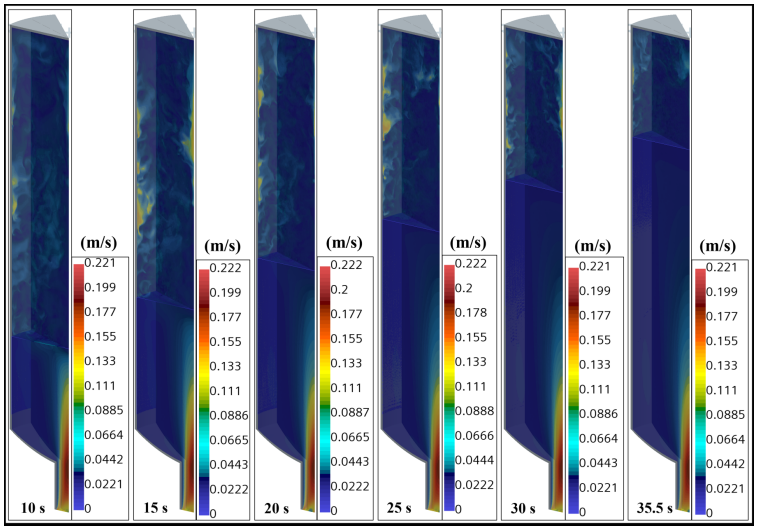

Figure 37. Velocity magnitude contours of CO_2 and PG within the chamber at t = 10, 15, 20, 25, 30, and 35.5 s. Results were obtained from the LES calculation of the compression process using a constant wall heat flux condition.

3.1.5 Conclusions of the Numerical Study of an LPC with Bottom Injection

Numerical simulations of an LPC in which the chamber filled with liquid PG from the bottom inlet to compress CO_2 were performed. The LES simulations coupled with the VOF model were used to simulate the transient interface between liquid PG and CO_2 gas and to capture the heat and mass transfers within the volume of the compression chamber. In this study, the effects of boundary conditions applied in the LES calculations, including no wall, an adiabatic wall, and a thick wall with a heat flux subscribed, were evaluated. In the results obtained from the LES calculation with no wall, no dynamical flow patterns were

observed in the chamber, the volume-averaged temperatures of CO_2 increased from 305 to 392.7 K, and the averaged gas velocity was between 2×10^{-3} and 3×10^{-3} m/s and remained stable during the compression process. On the other hand, LES calculations with a constant wall temperature or a wall heat flux had similar increases in CO_2 temperatures (maximum difference of 1.6 K). In these cases, the peak CO_2 velocity was 3×10^{-2} m/s at 11.4 s and gradually reduced to 2.1×10^{-2} m/s when the compression process finished. The results of the LES simulation with a wall heat flux revealed different stages in the compression process of the LPC, and the computed temperature and velocity fields showed that dynamic and complex patterns transiently occurred in the chamber. Because of the heat transfer between the solid wall and CO_2 gas, thin layers of colder CO_2 formed along the vertical and top walls. These layers moved downward, exchanged heat, expanded in width, and accelerated until they impinged into the liquid surface. After the impingement, the CO_2 gas layers diverged back into the gas volume and strongly enhanced the mixing phenomena inside the central gas region. The LES results also revealed circulation flow patterns within the chamber volume in which colder CO_2 gas layers moved downward along the side wall and warmer CO_2 gas volume moved upward in the central region. When the liquid level increased, the gas temperature increased rapidly because of the reduced heat transfer surface between the solid wall and gas layer as well as the gas volume at the top of the chamber. Future work will include experimental measurements performed on future prototypes, and the obtained results will be validated with numerical simulations.

3.2 NUMERICAL SIMULATION OF AN LPC WITH A SPRAY NOZZLE

This section summarizes numerical studies of an LPC in which PG liquid droplets were injected from the top to compress CO_2. Numerical simulations were performed using the unsteady Reynolds-averaged Navier–Stokes (URANS) approach coupled with a Lagrangian–Eulerian approach to simulate the transient heat- and mass-transfer processes between liquid PG droplets and CO_2 gas within the volume of the compression chamber. The commercial CFD package STAR-CCM+ 2021.1.1 was selected for this study. The heat-transfer and fluid-flow physics were a segregated coupling of flow and energy transport with the realizable k-ϵ turbulence model and two-layer all y^+ wall treatment. Interactions between the dispersed phase (PG droplets) and the continuous phase (CO_2 gas) were simulated using two-way coupling that allowed exchanges of momentum, heat, and mass between the phases. With two-way coupling, the effects of the dispersed phase on the continuous phase, such as displacement, interphase momentum, mass, and heat transfer, are taken into account.

The current STAR-CCM modeling capabilities are not able to simulate the transient processes of multiphase fluid mixtures, including liquid PG (representing the volume of liquid at the chamber bottom), CO_2 (representing the volume of gas at the chamber top), and liquid PG droplets (representing the dispersed phase suspended in CO_2 gas), with two-way coupling. In this study, the concept of a solid interface (i.e., a solid piston) moving with a constant speed was adopted to represent the interface between CO_2 and liquid PG at the chamber bottom. This concept enabled the numerical simulations using the URANS-Lagrangian approach with two-way coupling of PG droplets and CO_2 gas to be performed. The effects of injecting PG droplets into the chamber to compress CO_2 gas on the overall pressure, temperature, and the transient evolutions of flow, heat transfers, and mass transfers within the compression chamber were investigated and are discussed in the following sections.

3.2.1 Computational Domain

Figure 38 (left) shows the configuration of an LPC in which the chamber is filled using a spray nozzle. The x- and z-coordinates represent the horizontal planes, and the y-coordinate denotes the vertical direction. The origin of the coordinate system is the center of the chamber at a distance of $H_2 = 48.26$ mm from the bottom inlet. The compression chamber was designed to allow the entry of CO_2 from the top, and the compression fluid (i.e., PG) was initially filled in at $y = 0$ mm using the bottom inlet. The spray nozzle was installed at

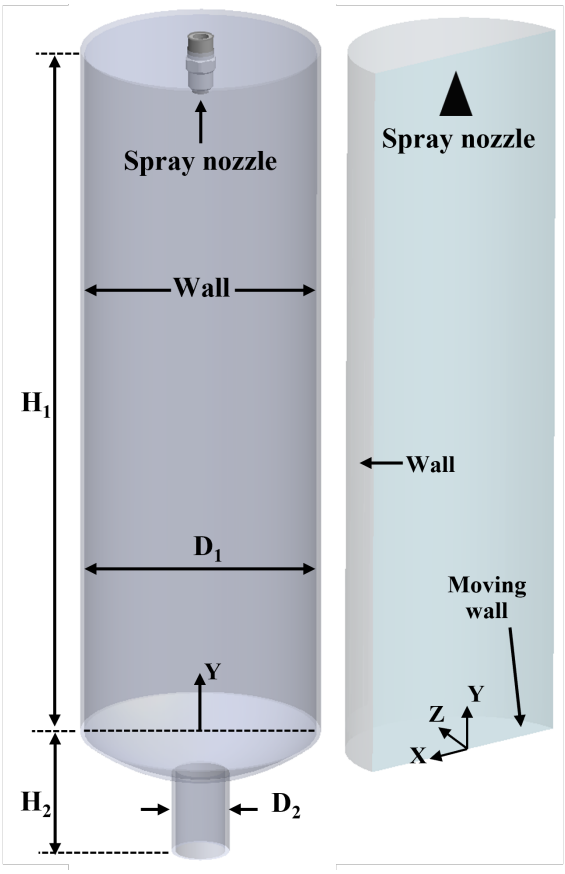

Figure 38. Design of an LPC with a top spray nozzle (left) and the computational domain used in the numerical study of the LPC (right).

the top of the chamber. In this study, the internal volume of the chamber was initially occupied by CO_2 gas, and the compression process started when liquid PG was sprayed into the chamber from the top with mass flow rates of Q_1 = 2 L/min and Q_2 = 3 L/min. The initial conditions of the chamber were a temperature of 305 K and a pressure of 2 MPa with the liquid PG level at the origin $y = 0$. The compression process stopped when the internal pressure of the chamber reached 8.6 MPa. To reduce the computational cost, the numerical domain of the compressing chamber was reproduced to a half portion with a symmetry plane as shown in Figure 38 (right). Because of the limitations of current modeling capabilities, the interface between CO_2 and liquid PG at the chamber bottom was modeled as a surface moving with a constant speed. This concept enabled simulations using an unsteady approach with two-way coupling of PG droplets and CO_2 gas. The thermal fluid flow phenomena within the chamber volume during the compression process were expected to be complex, involving unsteady compressible multiphase flow physics of liquid droplets and gas associated with conjugated heat transfer. During the compression process, liquid PG droplets were injected into the chamber at a constant mass flow rate while CO_2 gas within the chamber volume was compressed, making the gas flow patterns dynamically evolve and become very complex. During the compression process, interactions between PG droplets and CO_2 gas were simulated using two-way coupling that allowed exchanges of momentum, heat, and mass between the phases. The chamber's wall was specified as an adiabatic, no-slip boundary.

3.2.2 Numerical Modeling

In the studied configuration, numerical simulations of an LPC with droplet injection were performed using the URANS approach coupled with the Lagrangian–Eulerian multiphase approach to simulate the transient heat-

and mass-transfer processes between the injected liquid PG droplets and CO_2 gas within the compression chamber. The realizable k-ϵ turbulent model and two-layer all y^+ wall treatment were selected to calculate the heat-transfer and fluid-flow physics via a segregated coupling of flow and energy transport. The liquid phase of PG droplets was considered incompressible flow with a density of ρ_{ld} = 1,048 kg/m^3, a dynamic viscosity of μ_{ld} = 0.02678 Pa·s, a specific heat of $C_{p_{ld}}$ = 3,251 J/kg·K, a thermal conductivity of λ_{ld} = 0.2 W/m·K, a critical temperature of $T_{c_{ld}}$ = 626 K, a saturation temperature of $T_{sat_{ld}}$ = 460.75 K, a saturation pressure of $P_{sat_{ld}}$ = 7,871.66 Pa, and a surface tension of σ_{ld} = 0.0353 N/m. The gas phase was modeled as compressible multicomponent gas including CO_2 and PG vapor. The CO_2 gas had a specific heat of C_p = 850.566 J/kg·K, a dynamic viscosity of $\mu_{CO_2} = 1.49396 \times 10^{-5}$ Pa·s, and a molecular weight of 44.01 kg/kmol. The PG vapor had a specific heat of $C_{p_{lv}}$ = 76.095 J/kg·K, a dynamic viscosity of $\mu_{lv} = 1.164 \times 10^{-5}$ Pa·s, and a molecular weight of 76.095 kg/kmol.

In this study, the spray was continuously discharged into the chamber at a constant mass flow rate of 4.36 g/s. In the Lagrangian–Eulerian approach, governing equations for the continuous phase are expressed in Eulerian form and solved for flow fields, whereas injected droplets (particles) are tracked using the Lagrangian multiphase model. The turbulent fluid motion is governed by conservation of mass, linear momentum, and energy. Conservation of mass and momentum are given by Equations 17 and 18:

$$\frac{\partial \rho}{\partial t} + \nabla \cdot (\rho \boldsymbol{v}) = 0, \tag{17}$$

where ρ is the density and $\boldsymbol{v}$ is the continuum velocity; and

$$\frac{\partial (\rho \boldsymbol{v})}{\partial t} + \nabla \cdot (\rho \boldsymbol{v} \otimes \boldsymbol{v}) = -\nabla \cdot (p\boldsymbol{I}) + \nabla \cdot \boldsymbol{T} + \boldsymbol{f}_b, \tag{18}$$

where $\otimes$ denotes the outer product, $\boldsymbol{f}_b$ is the resultant of the body forces per unit volume acting on the continuum, and σ is the stress tensor. For a fluid, the stress tensor is often written as the sum of normal stresses and shear stresses, $\sigma = -p\boldsymbol{I} + \boldsymbol{T}$, where $\boldsymbol{I}$ is the identity matrix, p is the pressure and $\boldsymbol{T}$ is the viscous stress tensor.

Conservation of energy is given by Equation 19:

$$\frac{\partial (\rho E)}{\partial t} + \nabla \cdot (\rho E \boldsymbol{v}) = \boldsymbol{f}_b \cdot \boldsymbol{v} + \nabla \cdot (\boldsymbol{v} \cdot \boldsymbol{\sigma}) - \nabla \cdot \boldsymbol{q} + \boldsymbol{S}_E, \tag{19}$$

where E is the total energy per unit mass, $\boldsymbol{q}$ is the heat flux, and $\boldsymbol{S}_E$ is an energy source per unit volume. The Reynolds-averaged Navier–Stokes (RANS)–based approach to turbulence modeling was chosen for this study because of its relatively low computational cost compared with LES and direct numerical simulation. The temporal averaging methodology, or decomposition process, is to split fluid variables into their time-averaged means and fluctuating components.

To obtain the RANS equations, each solution variable ϕ in the instantaneous Navier–Stokes equations was decomposed into its mean (or averaged) value, $\bar{\phi}$, and its fluctuating component, ϕ':

$$\phi = \bar{\phi} + \phi', \tag{20}$$

where ϕ represents velocity components, pressure, energy, or species concentration. Applying this process to the previous three equations yields

$$\frac{\partial \rho}{\partial t} + \nabla \cdot (\rho \bar{\boldsymbol{u}}) = 0, \tag{21}$$

$$\frac{\partial}{\partial t}(\rho \bar{\boldsymbol{u}}) + \nabla \cdot (\rho \bar{\boldsymbol{u}} \otimes \bar{\boldsymbol{u}}) = -\nabla \cdot (\bar{p}\boldsymbol{I}_t) + \nabla \cdot (\bar{\tau} + \tau_{RANS}) + \boldsymbol{F_b}, \tag{22}$$

where ρ is the density, $\boldsymbol{I}_t$ is the identity tensor, $\bar{\boldsymbol{u}}$ is the mean velocity vector, $\bar{p}$ the mean pressure, $\bar{\tau}$ is the mean viscous stress tensor, and τ_{RANS} is the Reynolds stress tensor. The correlation between the fluctuating velocities is represented by the Reynolds stress tensor, $< u_i u_j >$, which is an unknown term, and a closure problem is required to model this stress tensor. One closure approach is based on eddy-viscosity models, which use the concept of a turbulent eddy viscosity, μ_t, to model the stress tensor as a function of mean flow quantities. The most common model is known as the Boussinesq approximation:

$$\tau_{RANS} = 2\mu_t \boldsymbol{S} - \frac{2}{3}\left(\mu_t \nabla \cdot \bar{\boldsymbol{v}}\right)\boldsymbol{I}, \tag{23}$$

where $\boldsymbol{S}$ is the mean strain rate tensor given by

$$\boldsymbol{S} = \frac{1}{2}\left(\nabla \bar{\boldsymbol{v}} + \nabla \bar{\boldsymbol{v}}^T\right), \tag{24}$$

and $\bar{\boldsymbol{v}}$ is the mean velocity.

In this study, the applied closure method was the realizable k-ϵ model containing a new transport equation for the turbulent dissipation rate ϵ (Siemens 2021). The k-ϵ turbulence model is a two-equation model that solves transport equations for the turbulent kinetic energy, k, and the turbulent dissipation rate, ϵ, to determine the turbulent eddy viscosity. Various forms of the k-ϵ model have been incorporated into Simcenter STAR-CCM+ (Siemens 2021). According to the STAR-CCM+ user's manual, the realizable k-ϵ model (Shih et al. 1995) is known to be very stable and to perform substantially better than the standard k-ϵ model (Jones and Launder 1972) for many applications. The realizable k-ϵ model contains a new transport equation for the turbulent dissipation rate, ϵ, and a variable damping function, f_μ, which is expressed as a function of mean flow and turbulence properties and is applied to a critical coefficient of the model, C_μ. This new approach allows the model to satisfy certain mathematical constraints on the normal stresses consistent with the physics of turbulence (realizability) (Siemens 2021). A two-layer wall treatment (Rodi 1991) was employed in combination with the realizable k-ϵ model. The two-layer approach facilitates application of the realizable k-ϵ model in the viscous-affected layer (including the viscous sublayer and the buffer layer). In Simcenter STAR-CCM+, the two-layer formulations work with either wall-function-type meshes $y^+ > 30$ when the mesh is not fine enough to solve the near-wall boundary layer or with low-Reynolds-number-type meshes $y^+ \approx 1$ when the mesh is fine enough to discretize the subviscous layer near the wall. The transport equations for the kinetic energy, k, and the turbulent dissipation rate, ϵ, are

$$\frac{\partial}{\partial t}(\rho k) + \nabla \cdot (\rho k \bar{\boldsymbol{v}}) = \nabla \cdot \left[\left(\mu + \frac{\mu_t}{\sigma_k}\right)\nabla k\right] + P_k - \rho(\epsilon - \epsilon_0) + S_k, \tag{25}$$

$$\frac{\partial}{\partial t}(\rho \epsilon) + \nabla \cdot (\rho \epsilon \bar{\boldsymbol{v}}) = \nabla \cdot \left[\left(\mu + \frac{\mu_t}{\sigma_\epsilon}\right)\nabla \epsilon\right] + \frac{1}{T_\epsilon} C_{\epsilon 1} P_\epsilon - C_{\epsilon 2} f_2 \rho \left(\frac{\epsilon}{T_e} - \frac{\epsilon_0}{T_0}\right) + S_\epsilon, \tag{26}$$

where $\boldsymbol{v}$ is the mean velocity; μ is the dynamic viscosity; σ_k, σ_ϵ, $C_{\epsilon 1}$, and $C_{\epsilon 2}$ are model coefficients; P_k and P_ϵ are production terms; f_2 is a damping function; and S_k and S_ϵ are the user-specified source terms. The realizable k-ϵ models provide a good compromise among robustness, computational cost, and accuracy. They are generally well suited to industrial-type applications that involve complex recirculation, with or without heat transfer. Previous studies related to multiphase droplet injections using these types of models include Ottosson (2019), Grandén and Persson (2020), Qin and Loth (2014), Qin et al. (2014), and Qin (2014).

In this study, PG liquid droplets were modeled as material particles and were assumed to have a spherical shape (i.e., they have mass and volume and are governed by the Lagrangian conservation laws of mass, momentum, and energy). Interactions between the dispersed phase (PG droplets) and the continuous phase (CO_2 gas) can be simulated via one-way coupling or two-way coupling. Coupling refers to the way that

momentum, heat, and mass are exchanged between the phases. With one-way coupling, the continuous phase influences the dispersed phase but not vice versa. The effects of the continuous phase on the dispersed phase are calculated by modeling the forces acting on the particles. With two-way coupling, the effects of the dispersed phase on the continuous phase, such as displacement, interphase momentum, mass, and heat transfer, are taken into account. Interactions between the dispersed phase and continuous phase are modeled. The Lagrangian equations can be solved for every single particle, but this requires significant computational resources for a large number of particles. In the Lagrangian multiphase approach, groups of particles that have the same properties, called parcels, are tracked by solving the Lagrangian equations of conservation of mass, momentum, and energy instead of by tracking each particle. This approach is more practical when the number of dispersed phases is large.

The conservation equation of momentum for a particle is written in the Lagrangian framework. The change in momentum is balanced by surface and body forces that act on the particle. The equation of conservation of (linear) momentum for a material particle of mass, m_p, is given by

$$m_p \frac{d\boldsymbol{v}_p}{dt} = \boldsymbol{F}_s + \boldsymbol{F}_b, \tag{27}$$

where $\boldsymbol{v}_p$ denotes the instantaneous particle velocity, $\boldsymbol{F}_s$ is the resultant of the forces that act on the surface of the particle, and $\boldsymbol{F}_b$ is the resultant of the body forces. In this study, these forces are decomposed into

$$\boldsymbol{F}_s = \boldsymbol{F}_d + \boldsymbol{F}_p, \tag{28}$$

$$\boldsymbol{F}_b = \boldsymbol{F}_g, \tag{29}$$

where $\boldsymbol{F}_d$ is the drag force, $\boldsymbol{F}_p$ is the pressure gradient force, and $\boldsymbol{F}_g = m_p \boldsymbol{g}$ is the gravity force, where $\boldsymbol{g}$ is the gravitational acceleration vector. The resultant of the surface forces, $\boldsymbol{F}_s$, represents the momentum transfer from the continuous phase to the particle. When using the two-way-coupling modeling approach, $\boldsymbol{F}_s$ is accumulated over all the parcels and applied in the continuous-phase momentum equation.

For the liquid PG droplets dispersed in CO_2 gas, the drag force, $\boldsymbol{F}_d$, is defined as

$$\boldsymbol{F}_d = \frac{1}{2} C_d \rho A_p \left|\boldsymbol{v}_s\right| \boldsymbol{v}_s, \tag{30}$$

where C_d is the drag coefficient of the particle; ρ is the density of the continuous phase; $\boldsymbol{v}_s = \boldsymbol{v} - \boldsymbol{v}_p$ is the particle slip velocity, where $\boldsymbol{v}$ is the instantaneous velocity of the continuous phase; and A_p is the projected area of the particle. In this study, the Liu dynamic drag correlation (Liu, Mather, and Reitz 1993) is applied to account for the dependence of the drag of a liquid droplet on its distortion under the action of aerodynamic forces. As a basis, it uses the following expression for the drag coefficient of an undistorted sphere:

$$C_d = \begin{cases} \frac{24}{Re_p}\left(1 + \frac{1}{6} Re_p^{2/3}\right), & Re_p \leq 1000 \\ 0.424, & Re_p > 1000 \end{cases}, \tag{31}$$

where Re_p is the particle Reynolds number that is defined as

$$Re_p = \frac{\rho \left|\boldsymbol{v}_s\right| D_p}{\mu}, \tag{32}$$

where D_p is the particle diameter and μ is the dynamic viscosity. As the distortion of the droplet increases, the droplet's shape is assumed to become a disk whose axis is aligned with the slip velocity. This shape increases the drag on the droplet. The Liu drag coefficient models this effect by noting that the high-Reynolds-number

limit of the drag coefficient of a disk is 1.54. It then assumes that the disk drag is 1.54/0.424 higher than the sphere drag at all Reynolds numbers and that the drag of intermediate shapes can be interpolated as

$$C_d = C_{d,sphere}\,(1 + 2.632y)\,. \tag{33}$$

The interpolation factor y is 0 for a sphere and 1 for a disk, and it can be identified using the Taylor analogy breakup (TAB) model, which is based on Taylor's analogy. The analogy represents a distorting droplet as a damped spring-mass system (Taylor 1940); it considers only the fundamental mode of oscillation of the droplet. The displacement and velocity of the mass in the spring-mass system correspond to representative distortion and rate-of-distortion quantities for the droplet. The TAB model equations govern the droplet oscillation and distortion (O'Rourke and Amsden 1987). When the droplet oscillations reach a critical value, breakup replaces the parent particles with child particles whose diameters are chosen from a Rosin–Rammler distribution.

The pressure gradient force, $\boldsymbol{F}_p$, is defined as

$$\boldsymbol{F}_p = -V_p \nabla p_{static}, \tag{34}$$

where V_p is the volume of the particle and ∇p_{static} is the gradient of the static pressure in the continuous phase.

A particle in turbulent flow experiences a randomly varying velocity field to which it responds according to its inertia. To model this effect, the turbulent dispersion model associated with the RANS turbulence model was applied. This model employs a stochastic approach based on a random walk technique to synthesize the fluctuating nature of the turbulent velocity field in the continuous phase. Following Gosman and Ioannides (1983), a particle is assumed to pass through a sequence of turbulent eddies as it traverses a turbulent flow field. Here, an eddy is a local disturbance to the Reynolds-averaged velocity field. The particle remains in the eddy until either the eddy timescale, τ_e, is exceeded or the separation between the particle and the eddy exceeds the length scale of the eddy, l_e. The particle experiences an instantaneous fluid velocity, $\boldsymbol{v}$, in each eddy, which is

$$\boldsymbol{v} = \bar{\boldsymbol{v}} + \boldsymbol{v}', \tag{35}$$

where $\bar{\boldsymbol{v}}$ is the local Reynolds-averaged velocity and $\boldsymbol{v}'$ is the eddy velocity fluctuation, which is modeled using a Gaussian distribution with a zero mean and a standard deviation given by the eddy velocity scale, u_e:

$$u_e = \frac{l_t}{\tau_t}\sqrt{\frac{2}{3}}, \tag{36}$$

where l_t and τ_t are the length scale and timescale of the turbulence, respectively. For the k-ϵ turbulence model applied in this study, the ratio of l_t/τ_t is $\sqrt{k}$.

When liquid PG droplets are injected into the compression chamber, interface heat and mass transfers occur between the droplets and CO_2 gas. The mass transfer is accompanied by interphase heat transfer, and the heat transfer can also occur because of the interphase temperature differences. The equation of conservation of mass of a material particle is given by

$$\frac{dm_p}{dt} = \dot{m}_p, \tag{37}$$

where m_p is the mass of the particle and $\dot{m}_p$ is the rate of mass transfer to the particle, which is zero unless mass transfer occurs, such as evaporation of droplets. With the injection of liquid PG droplets into the chamber, the temperature and pressure of the CO_2 gas increase and induce droplet evaporation. In this study, droplet evaporation was modeled using a quasi-steady single-component droplet evaporation model (Spalding

1960) that assumes droplets to be internally homogeneous, consisting of a single liquid component (PG in this study). The rate of change of droplet mass due to quasi-steady evaporation, $\dot{m}_p$, can be written as

$$\dot{m}_p = -g^* A_s \ln(1 + B), \tag{38}$$

where B is the Spalding transfer number and g^* is the mass transfer conductance, which represents geometrical and mechanical effects, such as the size and velocity of the droplet. The heat transfer limited evaporation mode was selected assuming that the vapor at the droplet surface was saturated and subcritical. This mode enforces a balance between latent heat transfer and other modes of heat transfer so that the droplet temperature remains at the saturation temperature at the droplet surface. Under this condition, the Spalding transfer number, B, is defined as

$$B = \frac{c_p\left(T - T_p\right)}{L}, \tag{39}$$

where L is the latent heat of vaporization. The mass transfer conductance, g^*, is defined as

$$g^* = \frac{kNu_p}{c_p D_p}, \tag{40}$$

where k is the thermal conductivity of the continuous phase, c_p is the particle specific heat, D_p is the particle diameter, and Nu_p is the Nusselt number.

The interphase heat transfer of droplets and gas can be expressed using the generic form of the conservation of energy equation:

$$m_p c_p \frac{dT_p}{dt} = Q_t + Q_{rad} + Q_s, \tag{41}$$

where Q_t represents the rate of convective heat transfer to the particle from the continuous phase, Q_{rad} represents the rate of radiative heat transfer, and Q_s stands for other heat sources. In the current study, radiative heat transfer and other heat source terms were not considered. The convective heat transfer, Q_t, is expressed as

$$Q_t = f h A_s\left(T - T_p\right), \tag{42}$$

where A_s is the particle surface area and h is the heat transfer coefficient. The factor f is a mass transfer correction (El Wakil, Uyehara, and Myers 1954) and is defined as

$$f = \frac{z}{e^z - 1}, \tag{43}$$

with

$$z = \frac{-\dot{m}_p c_p}{h A_s} \tag{44}$$

in the limit $\dot{m}_p \to 0$ and $f \to 1$. In this study, $f = 1$ was considered.

The heat transfer coefficient, h, is often given in terms of the particle Nusselt number and defined using a correlation as

$$Nu_p = \frac{hD_p}{k}, \tag{45}$$

where k is the thermal conductivity of the continuous phase. In this study, the Ranz–Marshall correlation (Ranz 1952), which is suitable for spherical particles up to $Re_p \approx 5{,}000$, was applied for defining the heat transfer coefficient as

$$Nu_p = 2\left(1 + 0.3 Re_p^{1/2} Pr^{1/3}\right), \tag{46}$$

in which Pr is the Prandtl number of the continuous phase. In this work, interactions between the PG droplets and CO_2 gas are modeled using two-way coupling to take into account the effects of the dispersed phase on

the continuous phase such as displacement, interphase momentum, mass, and heat transfer. The displacement of the continuous phase by the dispersed phase is accounted for through the volume fraction, ϕ_c. The volume fraction of a Lagrangian phase is the fraction of the local cell volume that phase occupies, and it is related to the available volume fraction for the continuous phase, ν, as follows:

$$\phi_c = 1 - \nu. \tag{47}$$

In two-way coupling, the rate of momentum transfer to a single particle, i, from the continuous phase is defined as

$$S_{v_i} = F_{v_i} + \dot{m}_{p_i} v_{p_i}, \tag{48}$$

where F_{s_i} is the force acting on the surface of the particle and $\dot{m}_{p_i}$ is the rate of mass transfer to the particle. The rate of total energy transfer to a single particle from the continuous phase is expressed as

$$S_{E_i} = Q_{t_i} + F_{s_i}.v_{p_i} + \frac{1}{2}\dot{m}_{p_i} v_{p_i}^2 + \dot{m}_{p_i} h, \tag{49}$$

where Q_{t_i} is the surface convective heat transfer, F_{s_i} is the surface force, and h is the enthalpy of transferred material. In the Lagrangian multiphase model, particles or droplets enter the computational domain through injectors at defined positions. Several types of injectors exist, such as part/surface injectors, point injectors, hollow/solid cone injectors, nozzle injectors, and table injectors. An injector has several parameters to define the properties of injected particles, such as size, velocity, temperature, and composition. In this study, a solid cone injector was applied with a negative y-axis, a circle cross section, an outer cone angle of 85°, a mass flow rate of 4.36 g/s, a particle temperature of 305 K, and a particle velocity of 16 m/s. A constant droplet diameter of 0.25 mm was considered. The time step was 0.001 s, and parcels were injected into the simulation domain at an injection rate of 100,000 parcels/s.

In this effort, a solid interface representing the interface between CO_2 and liquid PG at the chamber bottom was assumed to move with a constant speed. This modeling consideration enabled numerical simulations using the URANS-Lagrangian approach with two-way coupling of PG droplets and CO_2 gas.

3.2.3 Domain Discretization

The computational grid of the simulation domain (Figure 39) was generated using the automated mesh function in STAR-CCM+. In this effort, the surface remesher, trimmed cell mesher, and prism layer mesher were used. The surface remesher performed surface vertex retessellation of the imported 3D CAD to optimize surface faces based on the target edge length and proximity refinements. The trimmed cell mesher (hexahedral type) has been commonly recommended to apply with a multiphase flow model with moving boundaries because of the mesher's capabilities to create anisotropic cells, which best discretize the interfaces between the multifluids or multiregions/surfaces. Moreover, the trimmed cell mesher provides a robust and efficient method of producing a high-quality grid for both simple and complex mesh generation problems because it has highly desirable meshing attributes, such as predominantly hexahedral mesh with minimal cell skewness, refinement that is based upon surface mesh size and other user-defined refinement controls, surface quality independence, and alignment with a user-specified coordinate system. In general, in the trimmed cell mesher, growth rates control the rate at which cell sizes increase from one cell size to another within the trimmed cell mesh. The surface growth rate controls the rate of size changes between the cells that are next to surfaces and the cells in the core. The prism layer mesher generated a subsurface to extrude a set of prismatic cells from region surfaces into the core mesh. This layer of cells was necessary to improve the accuracy of the flow solution. The computational mesh was generated using a base size of 1 mm, a target surface size of 0.75 mm, a surface growth rate of 1.3, and refinements to the cell sizes in the vicinity of the moving surface (i.e., where the target surface size was 0.25 mm) and wall layers. Prism cells were applied in 12 layers in the near-wall region for a total thickness of 0.2 mm, and a prism layer near-wall thickness of 0.004 mm was used.

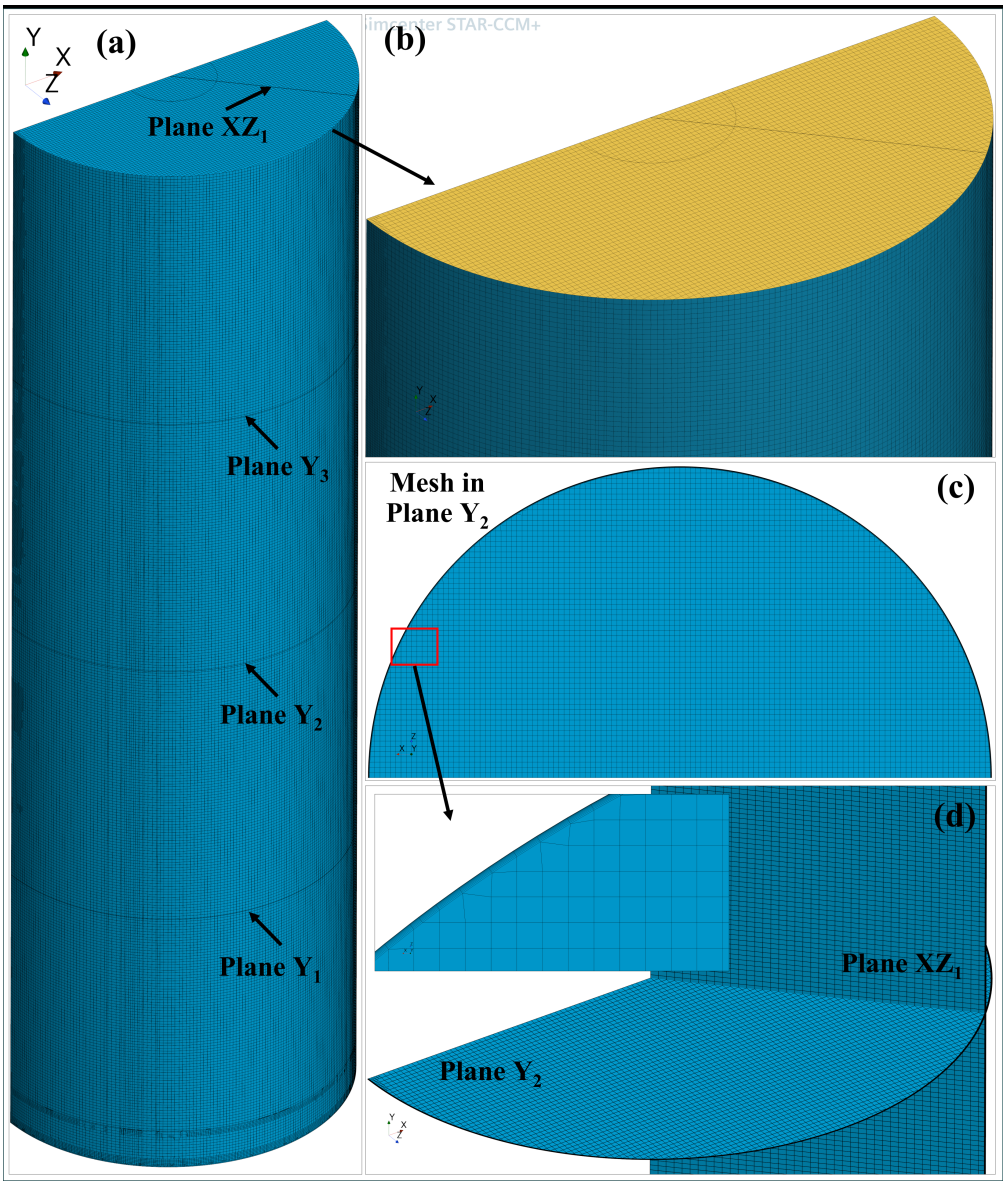

Figure 39. (a) and (b) Computational mesh generated with horizontal planes Y_1, Y_2, and Y_3 and vertical plane XZ_1; (c) mesh in plane Y_2; and (c) mesh in planes Y_2 and XZ_1.

3.2.4 Results and Discussion

This subsection describes results obtained from numerical simulations of a liquid compressor in which PG droplets were injected at the top of the chamber. CFD simulations were applied coupling URANS and Lagrangian approaches for liquid droplets and interactions (heat transfer) between the gas–liquid interface, droplets and gas, and the droplet–liquid interface. The liquid surface was simplified as a solid piston moving at a constant speed accommodating the total mass flow rate of liquid PG injected into the volume.

Figure 40 depicts the transient evolution of volume-averaged pressure and temperature and CO_2 gas within the compression chamber from t = 0 s to t = 25.4 s. Within the first 2 s, the CO_2 gas temperature reduced from 305 to 301 K and then slightly increased to 302 K before returning to nearly 301 K. After t = 8 s, the CO_2 gas temperature gradually increased from 300.2 to 311.5 K at t = 25.4 s, when the pressure reached

8.58 MPa. Compared with the overall CO_2 gas temperature increase of 50.15 K in the chamber during the compression process when the PG liquid was injected at the bottom, the gas temperature increased less than 7 K (approximately 2.2%). This could explain the effectiveness of the approach using droplet injection to achieve the near-isothermal condition of the LPC.

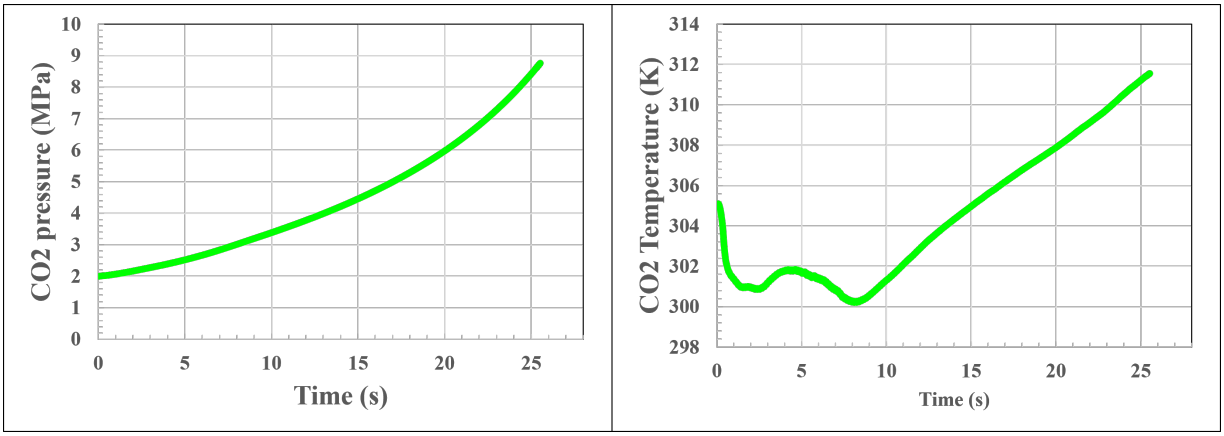

Figure 40. Pressure (left) and volume-averaged temperature (right) of CO_2 gas within the chamber during the transient compression process from 2 to 8.58 MPa. Results were obtained from the URANS calculation of the compression process using a spray nozzle at the top of the chamber.

Figure 41 shows temperature contours of the PG liquid droplets within the chamber during the compression process at various instants from t = 0.05 s to t = 25 s. In the initial period after the injection, the PG droplets moved downward to the bottom of the chamber, where the droplets exchanged heat with the CO_2 gas and decreased in temperature. This could explain the reduction of CO_2 gas temperature within the first 8 s as shown in Figure 40.

Figure 42 depicts the transient instantaneous velocity vectors of the PG droplets within the compression chamber from t = 0 s to t = 25.4 s. At the beginning of the injection, droplets moved downward and laterally spread out, possibly because of the use of a cone nozzle injector. In addition, a small portion of the droplets became suspended within the upper part of the chamber and moved upward, forming a pair of counter-rotating vortices along the central axis of the injection. After t = 0.5 s, the symmetrical formation of the vortex pair was no longer seen. On the other hand, after t = 1 s, the PG droplets created a circulation flow pattern within the chamber volume such that fast-moving droplets were observed on the top volume of the chamber and slower-moving droplets were observed at the bottom of the chamber. The large circulation flow pattern occurred on the top portion of the chamber and was maintained until t = 21.8 s. After that, no distinct flow pattern was observed within the compression chamber, and most injected droplets were located at the lower portion of the chamber.

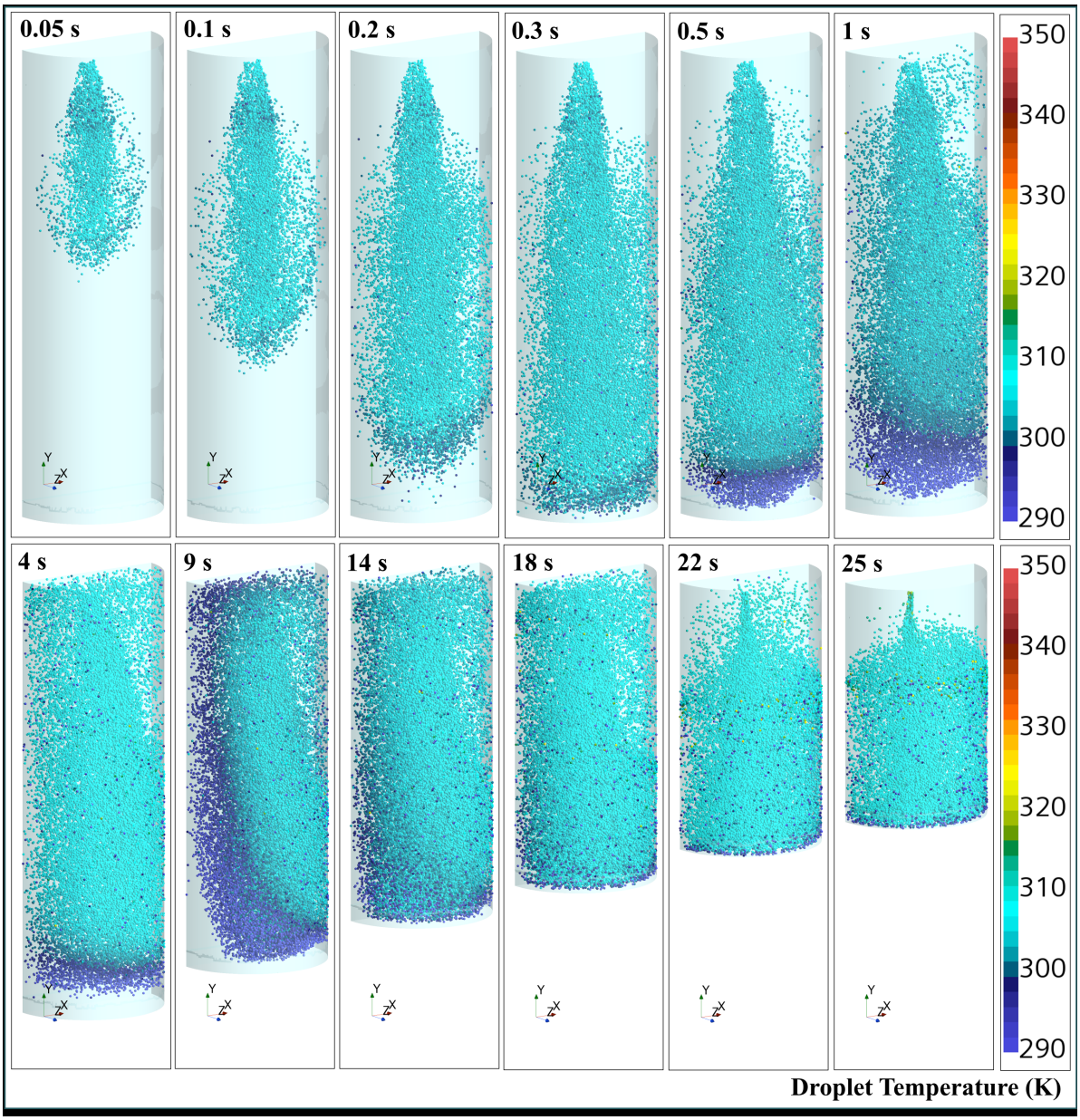

Figure 41. Temperature contours of PG droplets injected into the compression chamber at various instants from t = 0.05 s to t = 25 s. Results were obtained from the URANS calculation of the compression process using a spray nozzle at the top of the chamber.

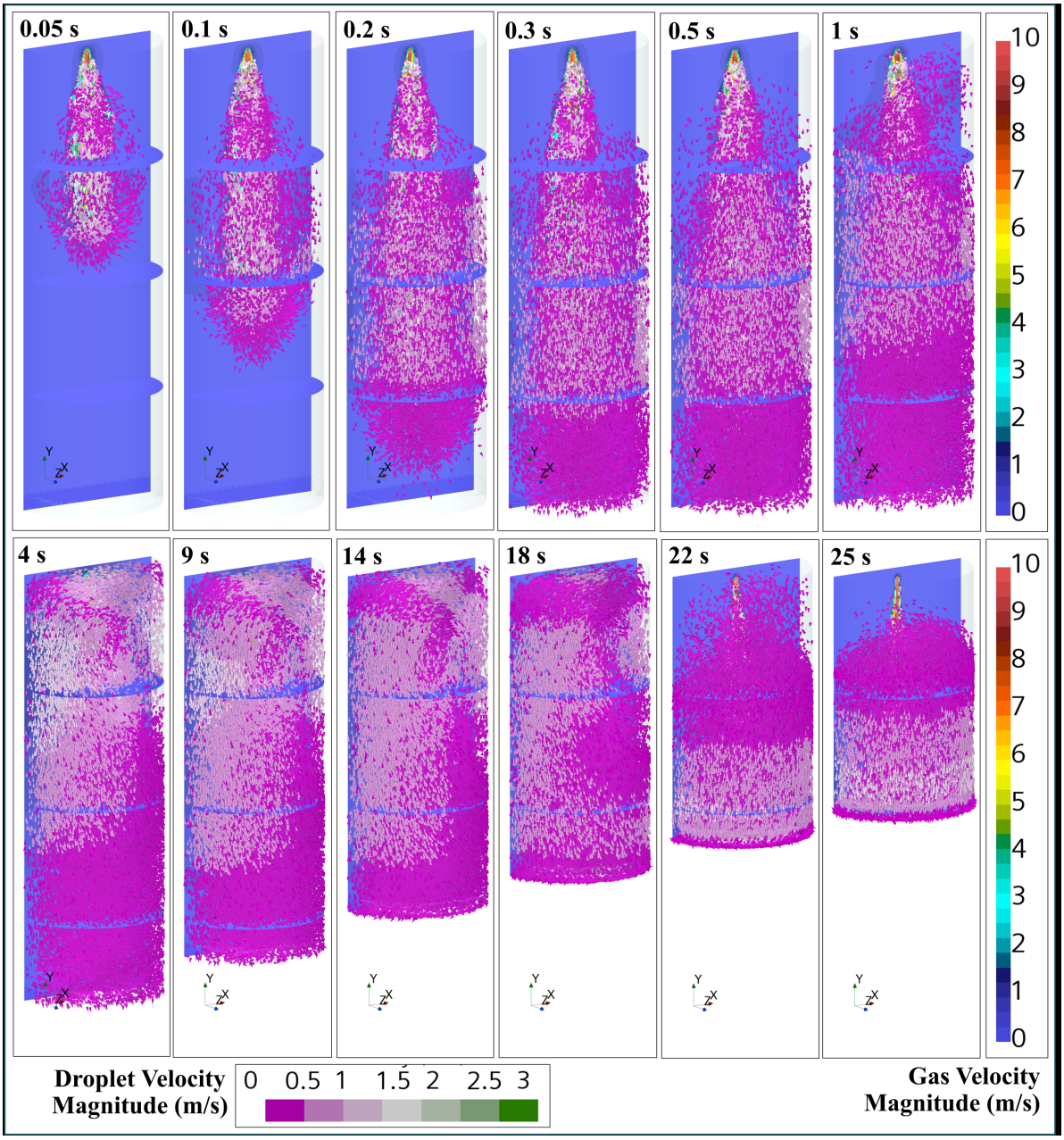

Figure 42. Velocity vectors of PG droplets and velocity magnitude contours of CO_2 gas within the compression chamber at various instants from t = 0.05 s to t = 25 s. Results were obtained from the URANS calculation of the compression process using a spray nozzle at the top of the chamber.

3.2.5 Conclusions of the Numerical Study of an LPC with a Spray Nozzle

Numerical simulations of an LPC in which a high-pressure spray nozzle was used to inject liquid droplets into the compression chamber to compress CO_2 were performed. A combined approach of URANS and Lagrangian–Eulerian modeling was applied to simulate the transient heat- and mass-transfer processes between the liquid PG droplets and CO_2 gas. The heat-transfer and fluid-flow physics were a segregated coupling of flow and energy transport with the realizable k-ϵ turbulence model. Interactions between the PG droplets and CO_2 were modeled using two-way coupling that allowed exchanges of momentum, heat, and

mass between the phases. The obtained CFD results showed that the CO_2 gas temperature increased less than 7 K (approximately 2.2%), demonstrating the effectiveness of the droplet-injection approach for achieving the near-isothermal condition of the LPC. The results also revealed the formation of counter-rotating vortices within the upper part of the chamber at the beginning of the droplet injection. After that, a large recirculation flow pattern was observed in the compression chamber, where fast-moving droplets were observed on the top volume of the chamber and slower-moving droplets were observed at the bottom of the chamber. The results of the model and initial comparison to experimental results demonstrate the need for further research. Specifically, further experimental measurements and flow visualizations are essential to verify and validate the results obtained from numerical simulations.

4. CONCLUSION

The goal of this project was to prototype and characterize the performance of a liquid-piston spray-cooled gas compressor. The working principle of the compressor enables optimized high-efficiency operation over a very wide range of operating conditions, unlike conventional compressors that are optimized for a narrow range of operating conditions. The compressor technology is suitable for many applications, such as gas pipeline transport, gas storage, and commercial and residential heat pumps. Physical testing and CFD modeling of the processes using the ORNL high-performance computing center were performed. The experimental and CFD studies focused on a near-isothermal LPC that used PG to compress CO_2.

Experiments were completed on a prototype with a single compression chamber and a prototype with two compression chambers. The results from the first prototype demonstrated near-isothermal compression. However, at higher CO_2 flow rates, the results of the experiments indicated significant carryover at compression speeds greater than 3 L/min. Although various nozzles seemed to reduce the amount of mixing, a large region of mixing was observed for all nozzles when the liquid level approached the nozzle. This mixing can be overcome with an additional switch of the fluid flow from the top to the bottom of the compression chamber. The prototype with two compression chambers did not provide useful results; the team was not able to operate the chambers sequentially because of unforeseen issues with the valve design.

In the first part of the simulation portion of this work, numerical simulations of an LPC in which the chamber filled with liquid PG from the bottom inlet to compress CO_2 were performed. The LES simulations coupled with the VOF model were used to simulate the transient interface between liquid PG and CO_2 gas and to capture the heat and mass transfers within the volume of the compression chamber. The effects of the boundary conditions applied in the LES calculations, including no wall, an adiabatic wall, and a thick wall with a heat flux subscribed, were evaluated. In the results obtained from the LES calculation with no wall, no dynamical flow patterns were observed in the chamber, the volume-averaged temperatures of CO_2 increased from 305 to 392.7 K, and the averaged gas velocity was between 2×10^{-3} and 3×10^{-3} m/s and remained stable during the compression process. On the other hand, LES calculations with a constant wall temperature or a wall heat flux had similar increases in CO_2 temperatures (maximum difference of 1.6 K). In these cases, the peak CO_2 velocity was 3×10^{-2} m/s at 11.4 s, and the velocity gradually reduced to 2.1×10^{-2} m/s when the compression process finished. The results of the LES simulation with a wall heat flux revealed different stages in the compression process of the LPC, and the computed temperature and velocity fields showed that dynamic and complex patterns transiently occurred in the chamber. Because of the heat transfer between the solid wall and CO_2 gas, thin layers of colder CO_2 were formed along the vertical and top walls. These layers moved downward, exchanged heat, expanded in width, and accelerated until they impinged into the liquid surface. After the impingement, the CO_2 gas layers diverged back into the gas volume and strongly enhanced mixing phenomena inside the central gas region. The LES results also revealed circulation flow patterns within the chamber volume in which colder CO_2 gas layers moved downward along the side wall and the warmer CO_2 gas volume moved upward in the central region. When the liquid level increased, the gas temperature increased rapidly because of the reduced heat transfer surface between the solid wall and gas layer as well as the gas volume at the top of the chamber. Future work will include experimental measurements performed on future prototypes, and the obtained results will be validated with numerical simulations.

In the second part of the simulation portion of this work, numerical simulations of an LPC in which a high-pressure spray nozzle was used to inject liquid droplets into the compression chamber to compress CO_2 were performed. A combined approach of URANS and Lagrangian–Eulerian modeling was applied to simulate the transient heat- and mass-transfer processes between the liquid PG droplets and CO_2 gas.

The heat-transfer and fluid-flow physics were a segregated coupling of flow and energy transport with the realizable k-ϵ turbulence model. Interactions between the PG droplets and CO_2 were modeled using two-way coupling that allowed exchanges of momentum, heat, and mass between the phases. The obtained CFD results showed that the CO_2 gas temperature increased less than 7 K (approximately 2.2%), demonstrating the effectiveness of the droplet-injection approach for achieving the near-isothermal condition of the LPC. The results also revealed the formation of counter-rotating vortices within the upper part of the chamber at the beginning of the droplet injection. After that, a large recirculation flow pattern was observed in the compression chamber in which fast-moving droplets were observed on the top volume of the chamber and slower-moving droplets were observed at the bottom of the chamber. Similarly to the first part of the simulation work, the results from the second part demonstrate that experimental measurements and flow visualizations are essential to verify and validate the results obtained from numerical simulations.

5. ACKNOWLEDGMENTS

This material is based upon work supported by the US Department of Energy Office of Energy Efficiency and Renewable Energy's Building Technologies Office under Contract No. DE-AC05-00OR22725. The authors would like to acknowledge Tony Bouza and Payam Delgoshaei, Building Technologies Office technology managers for HVAC, refrigeration, water heating, and appliances. Additionally, the authors would like to acknowledge the efforts of Tony Gehl, Brian Goins, Tim Dyer, and Josh Standifer in building the prototypes and Eric Loyd for designing the pressure vessel.

6. REFERENCES

Connell, Ken O, and Andrew Cashman. 2016. "Development of a numerical wave tank with reduced discretization error." In *2016 International Conference on Electrical, Electronics, and Optimization Techniques (ICEEOT),* 3008–3012. IEEE.

El Wakil, MM, OA Uyehara, and PS Myers. 1954. *A theoretical investigation of the heating-up period of injected fuel droplets vaporizing in air.* Technical report.

Gerstmann, J, and WS Hill. 1986. "Isothermalization of stirling heat-actuated heat pumps using liquid pistons." In *Intersociety energy conversion engineering conference. 21,* 377–382.

Gosman, AD, and E Ioannides. 1983. "Aspects of computer simulation of liquid-fueled combustors." *Journal of Energy* 7 (6): 482–490.

Gouda, El Mehdi, Mustapha Benaouicha, Thibault Neu, Yilin Fan, and Lingai Luo. 2022. "Flow and heat transfer characteristics of air compression in a liquid piston for compressed air energy storage." *Energy* 254:124305.

Gouda, El Mehdi, Mustapha Benaouicha, Thibault Neu, P Vergnol, Yilin Fan, and Lingai Luo. 2021. "2D versus 3D numerical modeling of flow and heat transfer in a liquid piston air compressor." In *ICNAAM 2021 19th International Conference Of Numerical Analysis And Applied Mathematics, Rhodes, Greece.*

Grandén, Anton, and Johan Persson. 2020. "Multiphase CFD simulation of water separation in automotive air intake systems." Master's thesis, Chalmers University of Technology.

Hirt, Cyril W, and Billy D Nichols. 1981. "Volume of fluid (VOF) method for the dynamics of free boundaries." *Journal of Computational Physics* 39 (1): 201–225.

Jones, W Peter, and Brian Edward Launder. 1972. "The prediction of laminarization with a two-equation model of turbulence." *International Journal of Heat and Mass Transfer* 15 (2): 301–314.

Liu, Alex B, Daniel Mather, and Rolf D Reitz. 1993. "Modeling the effects of drop drag and breakup on fuel sprays." *SAE Transactions,* 83–95.

Mechanical Engineers, American Society of. 2021. *ASME BPV Sec.VIII, Div.1 - Pressure Vessel Design.* Technical report. ASME.

Muzaferija, Samir. 1998. "Computation of free surface flows using interface-tracking and interface-capturing methods." *Nonlinear water-wave interaction. Computational Mechanics, Southampton.*

Neu, Thibault, Camille Solliec, and Bernardo dos Santos Piccoli. 2020. "Experimental study of convective heat transfer during liquid piston compressions applied to near isothermal underwater compressed-air energy storage." *Journal of Energy Storage* 32:101827.

Nicoud, Franck, and Frédéric Ducros. 1999. "Subgrid-scale stress modelling based on the square of the velocity gradient tensor." *Flow, turbulence and Combustion* 62 (3): 183–200.

O'Rourke, Peter J, and Anthony A Amsden. 1987. *The TAB method for numerical calculation of spray droplet breakup.* Technical report. SAE Technical Paper.

Odukomaiya, Adewale, Ahmad Abu-Heiba, Kyle R Gluesenkamp, Omar Abdelaziz, Roderick K Jackson, Claus Daniel, Samuel Graham, and Ayyoub M Momen. 2016. "Thermal analysis of near-isothermal compressed gas energy storage system." *Applied Energy* 179:948–960.

Ottosson, Oscar. 2019. “CFD simulation of urea evaporation in STAR-CCM+.” Master’s thesis, Linkoping University.

Patil, Vikram C, Pinaki Acharya, and Paul I Ro. 2020. “Experimental investigation of water spray injection in liquid piston for near-isothermal compression.” *Applied Energy* 259:114182.

Qin, CHAO. 2014. “Simulation of Spray-enhanced Compressed Air Energy Storage for Wind Turbines.” PhD diss., PhD dissertation). University of Virgina, School of Engineering and Applied . . .

Qin, Chao, E Loth, P Li, T Simon, and J Van de Ven. 2014. “Spray-cooling concept for wind-based compressed air energy storage.” *Journal of Renewable and Sustainable Snergy* 6 (4): 043125.

Qin, Chao, and Eric Loth. 2014. “Liquid piston compression efficiency with droplet heat transfer.” *Applied Energy* 114:539–550.

Ranz, William E. 1952. “Evaporation from Drops-I and-II.” *Chem. Eng. Progr* 48:141–146.

Rodi, Wolfgang. 1991. “Experience with two-layer models combining the k-epsilon model with a one-equation model near the wall.” In *29th Aerospace sciences meeting,* 216.

Schober, M, M Deichsel, and E Schlucker. 2016. “Computational fluid dynamics simulation and experimental validation of heat transfer in liquid piston compressors.” In *12th International Conference on Heat Transfer. Fluid Mechanics and Thermodynamics, HEFAT,* 511–516.

Shah, Ramesh K, and Dusan P Sekulic. 2003. *Fundamentals of heat exchanger design.* John Wiley & Sons.

Shih, Tsan-Hsing, William W Liou, Aamir Shabbir, Zhigang Yang, and Jiang Zhu. 1995. “A new k-epsilon eddy viscosity model for high reynolds number turbulent flows.” *Computers & fluids* 24 (3): 227–238.

Siemens. 2021. *StarCCM+ User Guide, Version 2021.1.* Siemens Simcenter.

Smagorinsky, Joseph. 1963. “General circulation experiments with the primitive equations: I. The basic experiment.” *Monthly weather review* 91 (3): 99–164.

Spalding, DB. 1960. “A standard formulation of the steady convective mass transfer problem.” *International Journal of Heat and Mass Transfer* 1 (2-3): 192–207.

Taylor, GI. 1940. “Generation of ripples by wind blowing over a viscous fluid.” *The Scientific Papers of GI Taylor* 3:244–254.

Tuhovcak, Jan, Jiri Hejcik, and Miroslav Jicha. 2015. “Modelling fluid flow in a reciprocating compressor.” In *EPJ Web of Conferences,* 92:02100. EDP Sciences.

Van de Ven, James D, and Perry Y Li. 2009. “Liquid piston gas compression.” *Applied Energy* 86 (10): 2183–2191.

Zhang, Chao, Mohsen Saadat, Perry Y Li, and Terrence W Simon. 2012. “Heat transfer in a long, thin tube section of an air compressor: an empirical correlation from CFD and a thermodynamic modeling.” In *ASME IMECE,* 45233:1601–1607.

Zhang, Chao, Jacob H Wieberdink, Farzad A Shirazi, Bo Yan, Terrence W Simon, and Perry Y Li. 2013. “Numerical investigation of metal-foam filled liquid piston compressor using a two-energy equation formulation based on experimentally validated models.” In *ASME IMECE,* vol. 56352, V08BT09A045.

Zhou, Qian, Dongmei Du, Chang Lu, Qing He, and Wenyi Liu. 2019. “A review of thermal energy storage in compressed air energy storage system.” *Energy* 188:115993.